Next Materials 6 (2025) 100329

Contents lists available at ScienceDirect

Next Materials

journal homepage: www.sciencedirect.com/journal/next-materials

Study of microstructure, phase and mechanical properties of a novel titanium aluminide-based alloy fabricated by direct energy deposition

Sadiq Abiola Raji[a,*], Abimbola Patricia Idowu Popoola[a], Olawale Muhammed Popoola[b], Sisa Leslie Pityana[c], Monnamme Tlotleng[c,d]

[a] Department of Chemical, Metallurgical and Materials Engineering, Tshwane University of Technology, Staatsartillerie Road, Pretoria West, P.M.B, Pretoria X680, South Africa
[b] Department of Electrical Engineering, Centre for Energy and Electric Power, Tshwane University of Technology, Staatsartillerie Road, Pretoria West, P.M.B, Pretoria X680, South Africa
[c] Laser Materials Processing Group, Photonic Centre, Council of Scientific and Industrial Research (CSIR), Pretoria 0001, South Africa
[d] Materials Science Innovation and Modelling Research Group, North-West University, Mahikeng, Mmabatho 2745, South Africa

ARTICLE INFO

Keywords:
Laser Engineered Net Shaping (LENS)
Direct energy deposition (DED)
Additive manufacturing (AM)
In-situ alloying
Titanium aluminide (TiAl) alloys
Ti-47Al-1.0Si-1.2Mo-8.0V at%
Computational modelling

ABSTRACT

Titanium aluminide (TiAl) alloy is deemed to possess desirable properties but exhibits significant drawbacks such as poor fracture toughness, wear and ductility that impedes its structural application and limit workability and production. Hence, it is crucial to accomplish a sufficient stability in relation to strength and ductility without losing other attractive material properties of the TiAl alloy. Therefore, this work is aimed at studying a novel TiAl-based alloy synthesized using direct energy deposition (DED) technique. The alloy was developed through in-situ alloying with Al, Si, Ti, Mo and V elemental powders to fabricate quintenary alloy of Ti-Al-Si-Mo-V. From the results obtained, it was observed that the microstructural and phase analysis of the Ti-Al-Si-Mo-V alloys exhibited varying amount of β_0 and ζ-Ti_5Si_3 phases along the grain interfaces reliant on the amount of Mo and V present with the formation of fully lamellar (FL) and duplex phase (DP) microstructures for 1400 °C and 1200 °C heat treatment temperatures, respectively. The Ti-Al-Si-Mo-V alloy ultimate tensile strength (UTS) was about 6.6–49.3 % greater than Ti-48Al-2 Nb-2Cr (GE-4822) alloy; while the yield strength (YS) was up to 34 % greater than GE alloy based on the nanoindentation results. Consequently, the Ti-Al-Si-Mo-V alloy would perform very well as material for aero-engines parts. The simulation result shows that cracking could be avoided by increasing the processing temperature. It was inferred that the processing temperature does not affect the maximum stress experienced by the TiAl alloy but the minimum stress level changes with processing temperatures.

1. Introduction

The most extensively used Ti alloys for aero-engine parts are titanium aluminides (TiAl) and Ti6Al4V alloys due to their outstanding properties. Nearly every aspect of mobility has made reducing weight a top priority in order to conserve energy, improve engine performance, and lower CO_2 emissions [1–4]. Compared to traditional titanium alloys, TiAl-based alloys have quite a few benefits including better modulus and specific strength, good creep properties, lower density (3.9 g/cm^3 to 4.2 g/cm^3), excellent strength-to-weight ratio, oxidation resistance up to elevated temperatures of approximately 750 °C and high strength at high temperatures [5–7], and superior resistance to oxidation owing to development of an alumina passivation film [8–10]. Over the years, Ti–Al alloy, generally indicated as gamma TiAl (γ-TiAl) alloy has been extensively investigated for applications in aerospace industry owing to their attractive characteristics. Hence, γ-TiAl alloys employed in a variety of high-temperature applications, including high-performance combustion engines and aircraft engine blades [6,11–18]. Consequently, Ti-Al alloys are recommended class of material for potential replacement of Ni-based super-alloys (density ~9 g/cm^3) for low-pressure turbine (LPT) blades and gas turbine engines of aerospace, automotive and energy applications [6,7,19,20–24] such as turbocharger wheels in car combustion engines, valves, and turbine blades in aircraft engines [1,15,25–28]. Prominent illustrations of their uses is the PW1000GTM and GEnxTM aeroengines LPT blades [24,29]. As a result, GEnx engines now weigh 100 kg less than before, and their fuel

---

* Corresponding author.
E-mail addresses: rajisadiqa@gmail.com, RajiSA@tut.ac.za (S.A. Raji).

https://doi.org/10.1016/j.nxmate.2024.100329
Received 23 March 2024; Received in revised form 15 June 2024; Accepted 22 July 2024

efficiency has improved by 20 %. Hence, TiAl alloys has drawn considerable attention of investigators in recent years as an emerging contender for innovative high temperature applications in the automobile and aerospace industries.

However, the main disadvantages of employing traditional production methods like forging and extrusion for fabricating γ-TiAl alloys is their limited workability, room temperature (RT) ductility [7,9,19,20] poor oxidation at temperatures above 800 °C, and inadequate fracture toughness [6,7,30,31]. This impedes their usage for engineering parts having complicated geometries via traditional processing technologies [11,32],. Also, the application of TiAl is restricted owing to an increase in the manufacturing costs [10] and technical hitches when it is being machined due to its inherent brittle nature, thus, making it problematic to process [33]. So as to expand the usage of γ-TiAl alloys, different TiAl have been conceived over time. Among these alloys, the most renowned being Ti-48–2–2 (Ti-48Al-2Cr-2 Nb, also called GE), which has a fracture strain of roughly 3 % at RT and being used by General Electric (GE) for LPT blades. Additionally, the Ti-43.5Al-4 Nb-1Mo-0.1B (TNM-B1) alloy, that has been used as jet engines of geared turbofan (GTF) LPT blade since 2016, has an RT fracture strain of roughly 1.2 % for cast components following heat treatment [4]. PW1100G-JM engine by Leistritz Turbinentechnik GmbH was successfully forged from Ti-43.5Al-4 Nb-1Mo-0.1B (TNM) alloy as turbine blades [22]. However, even with all these achievements, it is still problematic to process TiAl alloys into component owing to poor hot deformability and insufficient RT ductility that extremely restricts its real-world implementation.

Numerous efforts have been made, particularly in the area of alloy development, to increase workability and ductility of TiAl alloys. Metallurgical interventions, including thermomechanical treatment, alloying and microstructural modifications have been implemented to enhance RT fracture toughness and ductility. Micro-alloying with one or more alloying element such as Ta, C, Si, W, Mn, B, Mo, V, Cr, Nb, Ta and Zr (0.1–10, at%) [2,34–36] are suggested to be an efficient technique for improving TiAl alloys properties. The alloying elements' effects on TiAl-based alloys microstructures has drawn the attention of numerous researchers recently in an effort to enhance the mechanical and technical qualities [2,15,32]. However, the processing of TiAl is complex and remains the major challenge restricting the wider adoption of this appealing material. As a result, researchers are seeking novel methods to process TiAl alloys, hence, the development of a rather recent and innovative production process called additive manufacturing (AM) [37].

AM is a method of manufacturing three-dimensional (3D) parts from powder materials layers upon layers. This is becoming a crucial fabrication technique in medical, automotive and aerospace industries [38]. AM is an emerging technology that permits the production of near-net-shaped intricate components within a relatively short period of time at lower costs and higher efficiency in comparison to traditional production methods [11,39,40]. Directed energy deposition (DED) and powder bed fusion (PBF) methods are the two foremost categories of AM based on the material deposition techniques [41,42]. Powder particles are sprayed onto a substrate using a nozzle in the DED process, and melted along a predetermined computer-aided design (CAD) path by a high-power focused laser or beam, but for PBF process, the powder to be melted are pre-placed before the beam or laser melts the powders based. In recent times, interests in AM has increased considerably amongst industrial and academic experts due the capacity of manufacturing near net-shaped parts with unique properties that could not easily be achieved via traditional processes [38,43,44]. Moreover, since TiAl-based alloys is challenging to fabricate through traditional processes because of their intense brittleness. Thus, γ-TiAl alloy components are now being fabricated using AM processes like DED and PBF. In particular, lots of studies are now focused on γ-TiAl alloy fabrication processes of direct metal deposition (DMD), selective laser melting (SLM) and electron beam melting (EBM).

Lin et al. [24], examined the anisotropic Ti-48Al-2 Nb-2Cr alloy's tensile properties and microstructures fabricated by EBM followed by heat treatments after hot isostatic pressing (HIP). The alloy fabricated via EBM after HIP displays fine grains microstructural layers having high concentrations of α_2-phase that reveals a perpendicular build direction and (0001) strong texture causing the lamellae preferential orientation. Hoosain et al. [45], fabricated γ-TiAl clads from elemental powders of Al and Ti by DED altered by manipulating the Al powder feed rate while Ti is kept constant. The results of microhardness were significantly affected by changes in Al contents but heat treatment had no effect. Rittinghaus et al. [46], reported the microstructure and microhardness of Ti-43.5Al-4 Nb-1Mo-0.1B alloy fabricated via casting and laser metal deposition (LMD). It was realized that owing to composition disparities, minor fractions of β_0 were noticed in the LMDed alloy leading to lesser microhardness at RT. LMDed alloy microstructure had partially larger lamellar spacings because annealing occurred in the dual-phase field. Li et al. [47], investigated the correlations amongst the laser scan, nano-hardness and microstructural features of SLM processed TiAl/RGO metal matrix composites (MMCs). The average grain size during SLM processing of MMC was largely refined by increasing the line spacing of the laser scans. Likewise, B2 and γ contents increases while the α_2 phase content declines with increased line spacing of laser scans. The Young's modulus rises from 155.62 ± 7.78 GPa to 179.02 ± 8.90 GPa while the nano-hardness changes from 8.13 ± 0.39 GPa to 9.85 ± 0.46 GPa as line spacing of laser scans increases. Li et al. [48], investigated SLM-produced Ti-45Al-2Cr-5 Nb alloy with varying scan speeds of 800, 700, 600 and 500 mm/s. It was identified that SLM alloys showed randomly distributed γ phases and B2 within the matrix of α_2. The amount of α_2 phase decreases, as phases of B2 and γ increases as scan speed increases. As scan speed increases from 500 to 800 mm/s, nano-hardness rises from 7.90 ± 0.32 GPa to 9.49 ± 0.46 GPa, while the alloy's compressive characteristics increase from 829.41 ± 24.88 MPa to 1216.16 ± 36.48 MPa. Yue et al. [49], studied the influence of beam streaming on mechanical properties, misorientation of the grain boundaries, phase composition and microstructure of Ti-47Al-2Cr-2 Nb alloy produced via selective electron beam melting (SEBM). The findings showed that by changing the current beam to 8.5 mA from 4.5 mA, near-gamma (NG or near-γ) microstructure is produced from fine dual-phase (DP or duplex phase) structure. Also, the B2 and α_2 phase content increases while the γ phase volume fraction decreases and an increment of 330.45 Hv to 368.98 Hv were recorded for microhardness. Baudana et al. [50], performed a feasibility experiment to fabricated Ti-48Al-2 Nb-0.7Cr-0.3Si alloy via EBM followed by a suitable heat treatment strategy to achieve required microstructures. The components produced had few amounts of defects and were fully densified with about 2 wt% Al was observed to be loss. But Al loss could be compensated by using Al-enriched powder. The impurities content was comparable and very low between parts and powder representing the neatness of the procedure. Todai et al. [51], examined the deformation tensile properties and microstructure of Ti-48Al-2Cr-2 Nb alloy fabricated via EBM. EBM followed by repetitive localized heat treatment results in the creation of a distinctive microstructure comprised of γ bands and duplex-like regions. The alloy's yield strength (YS) and tensile elongation differed considerably subject to loading direction and building direction angle θ. All the studied samples at 800 °C showed good ductility of over 40 % and high YS above 350 MPa.

Additionally, a number of studies have examined the processing difficulties associated with AM of TiAl alloys. Gao, Wang and Zeng [52], examined the significances of parameters on crack sensitivity, characteristics and morphology of Ti-40Al-9 V-0.5Y alloy fabricated via SLM. The laser energy density is decreased by increasing layer thickness, defocusing distance and scanning velocity thereby resulting in higher clads sensitive to cracking. The optimum parameters for single tracks of Ti-40Al-9 V-0.5Y alloy fabricated via SLM were attained based on molten pool features and morphology of surfaces, thus, stipulating a useful indication for the creation of parts without cracking. Doubenskaia et al. [53], produced TiAl-4822 alloys through the SLM process by preheating the powder and varying the parameters of the process. The parametric analysis showed that modest speed results in reduced porosity and the higher thermal effect increases propagation and formation of cracks. Sharman, Hughes and Ridgway's [54], demonstrate that crack-free TiAl by laser additive manufacturing (LAM) could be fabricated without a secondary heat source. This was achieved by preheating the powder through defocusing the laser over the deposition plane. Thus, decreasing the rate of cooling lesser than the critical point for crack initiation. In the work of Tlotleng and Pityana [55] research, γ-TNB alloy was manufactured via AM in-situ alloying technique. It was observed that the studied samples showed porosities, cracks and unidentified microstructure prior to heat treatment. However, microstructure after heat treatment reveals lamellar with micro-grains observed to have no pores, refined and homogenous. This shows that α_2 phase deconvolution and precipitation was caused by heat treatment and γ-phase intensity thought to have a distinctive phase peak in the alloy.

The DED technique, is the focus of this work, which has several names, the majority of which are brand names of the several machine makers or research facilities. Among these are laser metal deposition (LMD), laser engineered net shaping (LENS), direct laser metal deposition (DLMD), direct laser deposition (DLD), and direct metal deposition (DMD) [54,56]. In contrast to typical manufacturing methods, the DED manufacturing process has a complex thermal history that can result in the production of unique microstructure, non-equilibrium phases, and significant residual stress [24,26,57,58]. However, the most significant problem with AM of TiAl alloys has been cracking due to the rapid cooling rates (104–106 K/s) associated with the process [6,57]. In the interim, it appears that a workable solution to prevent thermal shock cracking in Ti-Al constructions is to employ heating beds or pre-heat the base plates before fabrication. Heat treatment afterwards is required to relieve residual stresses and transform the microstructure. Nevertheless, DED offers an advantage of producing alloys by using wires, pure powders, or a combined feedstock called "in-situ" laser melting technique instead of the pre-alloyed powders. This shows that the DED technology is a cutting-edge manufacturing method that can be produced metallic structures with tailored properties that are adaptable for specialized applications.

Since the curiosity in TiAl-based alloys has increased vastly but applications seem to be limited due to processing problems in manufacturing parts. Therefore, this current investigation is focused on the fabricating of an innovative Ti-Al-Si-Mo-V alloy via the DED LENS technique. The goal is to produce γ-TiAl-based alloys that will display improved engineering performances. Nonetheless, akin to other highly robust and fragile materials, the primary obstacle of γ-TiAl alloys is their processability due to their high sensitivity to cracking. From reviewed literatures, it is clear that there are significant knowledge gap in the field of in-situ Ti-Al alloy production from their elemental powders using the DED process. The challenge of cracking could also be solved with the introduction of continuous heating during fabrication but not all the AM techniques are amenable to heat during processing. Moreover, most AM processes make use of pre-alloyed powders for the fabricating parts making the material's properties difficult to manipulate for specialized purposes. However, in this study, DED in-situ alloying is used because it allows for the adoption of elemental deposition of powders. In this case, the alloys were tailored for the manufacturing of improved performance of the TiAl-based alloys from elemental powders. Therefore, this investigation is focused on the development of innovative TiAl-based alloy through in-situ deposition of Al, Ti, Si, Mo and V by means of the a modified Optomec 850 R LENS machine system. Consequently, in-situ alloying powder deposition was adopted in this work to tailor the anticipated microstructure with enhanced mechanical properties.

2. Computational modelling

2.1. COMSOL multiphysics® package

COMSOL Multiphysics software version 5.5 was employed to build a model for the DED processing of TiAl alloy. This was adopted to determine predictive observation of the thermal stress and deformation with qualitative inferences validated by the experimental results. The model development, implementation and solution strategy are presented along with the model results which was validated by the experiments carried out.

2.2. Model strategy or approach

The main challenge in developing a model is providing adequate information on the anticipated component and processing to make enlightened engineering decisions. This work used a 3D model to predict the transient temperature profile and thermal stress of TiAl alloy by means of the heat transfer in solids module and structural mechanics physics of the COMSOL Multiphysics 5.5. A good predictive model should run in a realistic amount of time and produce reliable results defined by satisfactory physics. The ultimate aim of process modelling is to produce a system that can be effectively adopted and automated for process optimization [59]. Computational modelling helps to reduce manufacturing time and costs through the prediction of expected inconsistencies owing to the complicated thermal history of AMed products [60]. To simulate the effects of the processing temperatures on a 3D printed part. A transient solution was adopted by selecting a parametric solver. The laser processing parameters used for the simulations study is itemized in Table 1. The properties of the material are derived from existing literature and are deemed to be isotropic. The linear system was solved using the parallel sparse direct solver (PARDISO). A significant movement solution is permitted when the "large deformation" box is enabled. The augmentation components and the segregated solver are part of the arbitrary lagrangian-eulerian (ALE) approach utilized to solve the interfaces.

2.3. Governing equations

The central component of any AM process model is the model heat source. This is expressed in numerical term to denote how the heat source essentially heats the metallic powders including its distribution along the heat-affected zone (HAZ). AM modelling of heat sources is somewhat similar to welding while the main difference is that AM entails building on a layer-by-layer basis but fundamentally the heat source relations with the surface are identical. Eq. 1 was used to calculate laser beam energy density of DED during deposition.

$$E = \frac{P}{Vd} \tag{1}$$

where E: laser beam energy density (J/mm^2), P: power (Watts), V: laser scan speed (mm/s), and d: laser spot size diameter (mm). The distribution of power by the laser beam heat source is depicted using the Gaussian distribution model. The heat source adopted in this work is a

Table 1
Laser Processing Parameters used for the Simulation.

Expressions	Values
Laser Power (W)	450
Laser Scanning Speed (mm/s)	10.58
Laser Spot Size (mm)	5
Position of the Focus (mm: origin;- x, y, z)	20, 40, 5
Size of Sample Model (mm)	40 ×80 x 15
Distance Between Two Layers (mm)	5
Distance of z-Increment Between Two Successive layers (mm)	5

Gaussian heat source expressed in Eq. 2, stated as energy per area (thermal flux density). The Gaussian distribution represents the DED processing as a moving heat source.

$$f = \frac{2 * Power}{\pi r^2} e^{\left(-2\frac{x^2+y^2}{r^2}\right)} \tag{2}$$

where f: heat flux (J/mm^2), r: laser spot size radius (mm), Power: power (Watts), y and x: variables representing the laser beam distance from the build center. The laser beam Gaussian distribution and the heat source Gaussian cone are presented as Supplementary Material 1. The Gaussian distribution is a 2D representation along the x-y direction that penetrates linearly along the z-axis presented in Fig. 1b. Thus, making the model distinct from Goldak's ellipsoidal model [60]. When using finite element analysis (FEA) technique to evaluate temperature fields of LAM, the model heat source is helpful. Based on the principle of heat transfer (in solids), the 3D transient temperature field heat source for the TiAl proceeded by DED was determined by the Fourier heat differential equations (Eqs. 3 and 4):

$$\rho C_p \frac{dT}{dt} + \rho C_p u \ . \ \nabla T + \ \nabla \ . \ q = Q + \ Q_{ted} \tag{3}$$

$$q = -k\nabla T \tag{4}$$

where ρ: density (kg/m^3), C_p: specific heat (J/Kg/K), t: time (seconds, s), T: temperature (Kelvin, K), Q: heat source intensity (J/mm^2) and k: thermal conductivity coefficient (W/m.K); while k and C_p are temperature dependent. Similarly, structural deformation mechanics of the 3D laser processing was predicted using Eq. 5. This is applied to ascertain the properties of the material to deformation flow and stresses as a result of heat accumulation during processing.

$$\rho \frac{\partial^2 u}{\partial t^2} = \nabla . S + F_v \tag{5}$$

where ρ: density (kg/m^3), F: linear transformer, t: time, S: translational transformer and u: vector quantity.

In the modelling of computational fluid dynamics (CFD) processes, one main challenge encountered is the determination of local variables changing with temperatures which lead to surface tensions. These differences lead to Marangoni flow in liquids that considerably determine melt pool depth and shape [59]. This model does not contain the gas phase around the substrate owing to a great disparity in dynamic viscosities and densities between the gas and melt pool. In restraining the speed of the solid region, this model utilizes a Darcy condition involving the equation of mass conservation (Eq. 6), equation of momentum conservation (Eq. 7) and energy conservation equation (Eq. 8). This pertains to the melt pool area, solid phase and liquid phase assuming the fluid flow is laminar and a Newtonian fluid.

$$\frac{\partial \rho}{\partial t} + \ \vec{\nabla} \ \bullet (\rho V) = 0 \tag{6}$$

$$\rho C_p^* \left(\frac{\partial T}{\partial t} + \ (\vec{u} - \ \vec{u}_m) \ \bullet \ \vec{\nabla} T \right) = \ \vec{\nabla} \ \bullet \ (k \vec{\nabla} T) + \ Q_v \tag{7}$$

$$\rho_o \left[\frac{\partial \vec{u}}{\partial \vec{t}} + \ ((\vec{u} - \ \vec{u}_m) \ \bullet \ \vec{\nabla}) \ \vec{u} \right] = \ \vec{\nabla} \bullet \ \left[-pI + \ \mu_o \ \left(\vec{\nabla} \vec{u} + \ (\vec{\nabla} \vec{u})^T \right) \right] + \ \vec{F}_{Bouyancy} + \ F_{Darcy} \tag{8}$$

where p: pressure (Pa), T: temperature (K), k: thermal conductivity (W/m/K), ρ: density (kg/m^3), Q_v: heat source (W/m^2), C_p*: equivalent heat capacity (J/kg/K), ρ_o: density at $T = T_m$, $\vec{u}$: fluid velocity (m/s), μ_o: dynamic velocity (Pa*s) and $\vec{u}_m$: mesh velocity vector (m/s). At ambient air, heat loss owing to convection and radiation ensuing on the substrate is stated as thus in Eq. 9:

$$Q_v = \ -2 \frac{\left(h_c \ \ (T - \ T_0) + \ \varepsilon \sigma_B \ \ (T^4 - \ T_0^4)\right)}{W_o} \tag{9}$$

where W_o: substrate thickness, σ_B: Stefan-Boltzman constant, ε:

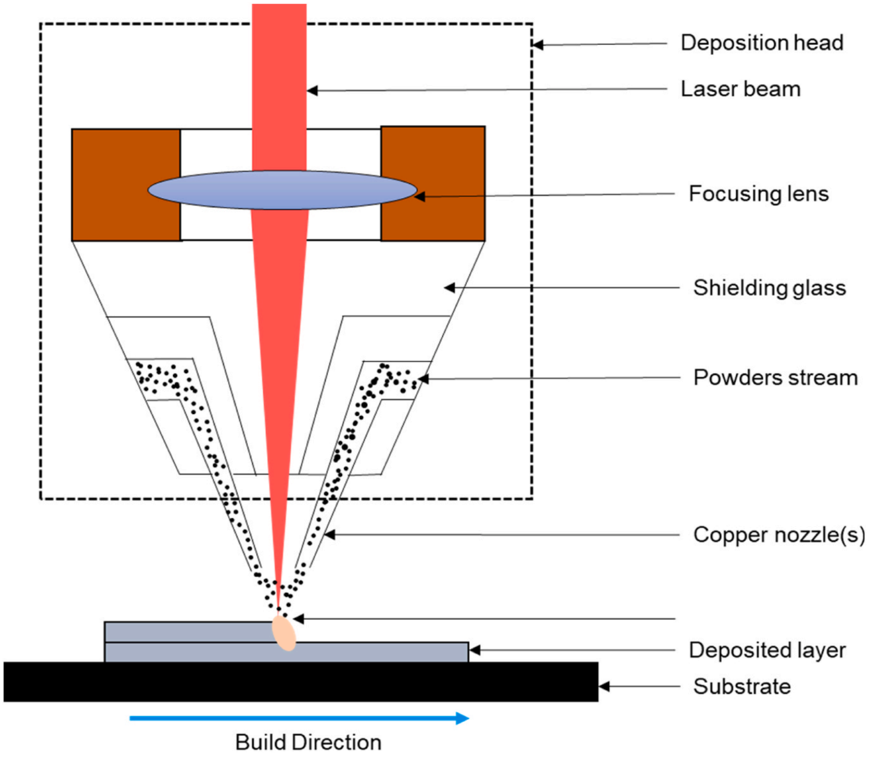

Fig. 1. Schematic Representation of DED Process at the Deposition Head.

emissivity, T_0: operating temperature and h_c: coefficient of heat convection. The Stefan-Boltzmann law is applied to define heat dissipation owing to radiation (where Stefan-Boltzmann constant is 5.67 10^{-8} W/m^2). Equivalent heat capacity is expressed in Eq. 10.

$$C_p^* = C_p \quad (T) + \frac{\Delta H_m}{\sqrt{\pi (T_L - T_S)^2}} \exp\left(- \frac{(T - T_m)^2}{(T_L - T_S)^2} \right) \tag{10}$$

where T_S and T_L: are solidus and liquidus temperatures, respectively, ΔH_m: latent heat of fusion (J/kg), and T_m: temperature at melting point (K). The DED process model exhibits distortion and residual stresses in build parts owing to heat transfer. This can be quantified by heat conduction Fourier's law (Eq. 11) in view of the repetitiveness of the AM process in layers:

$$\frac{\partial}{\partial x} \quad \left(k \frac{\partial T}{\partial x} \right) + \quad \frac{\partial}{\partial y} \left(k \frac{\partial T}{\partial y} \right) + \quad \frac{\partial}{\partial z} \left(k \frac{\partial T}{\partial z} \right) + q = \rho C_p \frac{\partial T}{\partial t} \tag{11}$$

where t: interaction time of powder and laser layer, q: system heat input rate, Cp: specific heat, ρ: density, T: continuum temperature, and k: thermal conductivity. Consequently, complete descriptive information of the process is vital to achieving reliable results when performing thermomechanical modelling like the DED process. The metallic powder thermophysical properties considerably influence the melt pool stability of the modelled process [61]. The measurements of temperatures through experiments are only limited to the surface temperatures. But the internal temperature cannot be measured in a straightforward manner. The melt pool small size, liquid motion controlled by Marangoni convection, rapid temperature change and moving heat source makes it problematic to accurately measure the transient temperature [62]. The expansion coupling was governed by Eq. 12, where α is the thermal expansion coefficient (1/K).

$$\in = \alpha(T) * (T - T_0) \tag{12}$$

2.4. *Material properties used in the model*

Materials' thermophysical properties have tremendous effects on the temperature regime that precisely controls the size and shape of components produced throughout the DED process. It is essential to state that the thermal properties of materials are temperature dependent, thus, widely accepted values in the literature of these various properties were used for this simulation study. These thermophysical properties are itemized in Table 2.

2.5. *Initial boundary conditions*

Convection is the primary source of heat loss in the DED process, and this was taken into account in the model study of heat transfer. Boundary conditions, which consider the heat source, radiation and convection losses are considered by Eqs. 3–5, are necessary for the simulation of the DED process. The initial temperature, T_0 of the base plate is set at 23 °C and 800 °C, while initial pressure and velocity field were set at zero. The heat transfer physics, radiation losses, convection and laser source are the boundary conditions considered. The energy distribution intensity is regarded as homogeneous and considers heat flux owing to the free boundary conditions in comparison to the incident laser beam.

Table 2
Thermophysical Properties of TiAl Alloy used in COMSOL Simulation.

Description	Values
Coefficient of Thermal Expansion (K^{-1})	8.6 $\times 10^{-6}$
Density of Material (liquidus) (kg/m^3)	3780
Density of Material (solidus) (kg/m^3)	3900
Heat Capacity of Material (J/(kg·K))	610
Thermal Conductivity (W/(m·K))	20
Young's Modulus (Pa)	1.68 $\times 10^{11}$
Poisson Ratio	0.22
Liquidus Temperature (K)	1807
Solidus Temperature (K)	1719
Thermal Transmittance (W/(m^2.K))	15

2.6. *Meshing*

The meshing of the laser-scanned regions and surroundings should be accurately subdivided while other regions is approximated. The model finite element meshing is presented as Supplementary Material 2. COMSOL Multiphysics® uses a hyper-elastic smoothing method in conjunction with the ALE method for the moving mesh. A free tetrahedral mesh element type is used with absolute tolerance of 10^{-3} and relative tolerance of 10^{-2}. The simulation was executed using a 16 GB RAM Windows 10 operating system computer taking a total time of 6 hours 33 minutes 13 seconds to complete. The results of finite element analysis (FEA) accurateness are largely determined by the size and pattern of the meshing system used during the investigation [61]. An adaptive mesh refinement (AMR) was adopted for multi-resolution approaches forming embedded grids at higher resolutions at regions of dynamic part distortions. AMR is a non-uniform meshing structure that can occupy the areas of concern with denser meshes [61].

2.7. *Model assumptions*

In any simulation study, assumptions are very important to lessen the complexities of the complete process under investigation. In this work, the assumptions that were made to make the model easy, direct and close to real-life situations as possible are that; (i) material vaporization was neglected for DED modelling, (ii) no conduction heat loss during the DED process, (iii) the material is isotropic, (iv) solidification is negligible, and (v) the material is linearly elastic and DED process flow function during melting.

3. Experimental

3.1. *Materials*

This study makes use of elemental CP powders of Al, Ti, Si, Mo and V as feedstock materials with Ti6Al4V alloy metal plate as the substrate. All materials were provided through vendors; WEARTECH (PTY) LTD, South Africa (Al, V and Mo) and TLS Technik GmbH & Co, Germany (Ti and Si). The as-received powders were all subjected to particle size analysis and examined with scanning electron microscopy with fitted electron dispersion spectroscopy (SEM-EDS). SEM micrographs of these feedstock materials are shown in Supplementary Material 3. All powders used in this work were in the expected range of 45–90 μm needed for processing in Optomec 850 R LENS machine.

As regards TiAl-based alloys Appel, Paul and Oering [62], reported that Mo improves oxidation properties, ductility and strength of fine-grained materials. While, 1–3 at% V addition rises the ductility of duplex TiAl-based alloys. It also results in the shifting the $(\alpha_2+\gamma)/\gamma$ to the Ti region and decreases Al content in the γ phase. Si increases fluidity, reduces susceptibility to hot cracking, refines cast microstructure and improves oxidation resistance. Addition of 0.5–1 at% Si improves creep resistance. When Si addition is in minor proportions below 1 %, ζ-Ti_5Si_3 phase precipitates and increases properties of TiAl alloys at elevated temperatures [63,64]. Hence, the rationale for the selection of Si, Mo and V as alloying elements for the reinforcement of the Ti-Al alloys developed.

3.2. *Methodology*

3.2.1. *Sample Fabrication*

The fabrication of samples was systematically developed based on the previous studies carried out by the Laser Enabled Manufacturing Group, Manufacturing Division, Photonic-Centre, Council of Scientific and Industrial Research (PC-CSIR), Pretoria, South Africa. The parameters of the Ti and Al were adopted from the published work of Tlotleng [65]. Thus, the parameters selected for the Al, Ti and Si powders are kept constant for this work and the laser processing parameters provided in Table 3 are used to produce the Ti-Al-Si-x(Mo+V) alloys. In this work, fabrication of TiAl-based alloys is carried out using an Optomec 850 R LENS machine (Albuquerque, NM, USA) which draws energy from a 1000 W IRE-Polus Group (IPG) laser fiber. Supplementary Materials 4 presents the Optomec 850 R LENS machine used at PC-CSIR, Pretoria, South Africa. The samples were deposited onto the metal plate substrates of Ti6Al4V alloy through in-situ laser alloy deposition of powders. The LENS machine deposition head has a four-way feeding nozzles made of copper which deposits powders co-axially on the base plate while a beam of laser instantaneously dissolves the powder materials. Optomec Application Launcher-Work Station Control Software Version 3.1.6 (Optomec, Albuquerque, NM, USA) automatically controlled the laser from the central computer workstation. Fig. 1 depicts the schematic representation of a typical DED technique at the deposition head when the laser melts the powders on the substrate. Realizing that Optomec 850 R LENS has only two powder feeds and that it is possible to accomplish in-situ laser alloying without premixing the powder materials. Using three externally attached powder feeders (GTV Verschleiss-Schutz Gmbh, Luckenbach, Germany), to supply the Si, V, and Mo powders while the Ti and Al powders were deposited by powder feeders of the LENS machine. This resulted in a five-way powder feeding system, as opposed to two that the manufacturer had originally installed. Therefore, our experiment design setup is a modified five powder feeders LENS system.

Owing to the cracking susceptibility of TiAl-based alloys during processing, a heating platform was incorporated into the LENS machine. It goes without saying that heat flows downward during the DED process, and delamination-intense cracking is anticipated to follow the layer heat profile from bottom to top when processing TiAl-based alloys. Taking into account phase diagram of typical binary Ti-Al in Refs [65, 66], fabricating Ti-Al on a substrate that is continually heated to maintain the built samples at temperatures below the recrystallization temperature and limit delamination due to cracking. A heating platform was introduced to control and/or reduce thermal gradient during sample fabrication based on our observation from the simulation results. The ceramic heating platform had a heating element and thermostat controller attached to it; this was used to continuously keep the temperature of the base plate constant to prevent cracking. Fig. 2 depicts the modified LENS schematic setup. The Ti6Al4V alloy substrates that were utilized were sandblasted and cleansed with acetone prior to deposition. The samples were built based on the pre-programmed CAD file using a cross-hatch pattern of deposition strategy along axes of x and y. The alloys were generated at a laser power of 450 W, 10.58 mm/s scan speed, and 25 l/min center purge gas rate. With the intention of varying the composition of alloy samples deposited, each elemental powder flow rates were approximated following calibration of the powder flow rate in rpm (revolution per minute) and converted to mass flow rate in g/min. In order to accomplish this, the powder feeders' rpm was changed.

Table 3
Laser Processing Parameters used for Producing Ti-Al-Si-x(Mo+V) Alloys.

Parameter		Values				
Scan Speed (mm/s)		10.58 mm/s				
Stand-off Distance (mm)		8.0 mm				
Centre Purge (l/min)		25 l/min				
Hatch Distance (mm)		0.675 mm (50 % overlap)				
Layer Thickness (mm)		0.2 mm				
Laser Spot Size (mm, diameter)		1.35 mm				
Laser Power (W)		450 W				
		Ti	**Al**	**Si**	**Mo**	**V**
Sample 1	Powder Feed Rate (g/min)	2.21	0.48	0.025	0.05	0.35
Sample 2	Powder Feed Rate (g/min)	2.21	0.48	0.025	0.05	0.50

3.2.2. *Heat treatment*

As a post-processing approach, heat treatment (HT) is known to relieve internal stresses of as-built samples while homogenizing their microstructure. The phase diagram of binary Ti-Al indicates that various HT temperatures and approaches could be employed to create various microstructures. This depends on how the alloy or composition is cooled as well as how much aluminium is present. The samples were heat-treated for 60 minutes at temperatures of 1200 °C and 1400 °C, with subsequent furnace cooling (FC). The heat treatment furnace (Kejia Furnace, China) was applied for the post-processing in an inert atmosphere having an inlet for the continuous supply of Ar (99.99 % purity) to prevent contaminations and oxidation during HT. After ramping the temperature from RT to the desired temperature at 20 °C per minute, FC was done after holding for 60 minutes at the set temperatures.

3.2.3. *Sample preparations*

To prepare samples for analysis, the fabricated samples are sectioned (before heat-treatment) using the Struers Discotom–5 (Advance Laboratory Solutions, South Africa) cutting machine. The machine is controlled manually and highly suitable for sectioning extensive range of materials. The sectioned samples are then mounted in phenolic resin by means of Press AMP 50 (Laryee Technology Co. LTD., China) automatic mounting press for preparation before characterizations. This was followed by manual grinding using grit papers starting with P4000, P1200, P320 and P80 grit size with subsequent samples polishing to achieve a mirror finished surface using OP-S suspension fluid. The Struers TegraForce-5 (Struers Inc, USA) grinding/polishing machine was used in this work for the grinding and polishing. To visualize the microstructure and phase analysis, Kroll's reagent—92 millilitres of distilled water (H_2O), 6 millilitres of hydrochloric acid (HCl), and 2 millilitres of hydrofluoric acid (HF)—was used as an etchant on the polished surface. Prior to beginning the etching process, acetone was used on polished surfaces following the polishing step in order to eliminate any potential contaminants. In order to ensure that there was no contamination, acetone was poured on the surface after the etching process. The surface was then dried up by means of a blower similar to a hair dryer. This was the first method used to prepare samples for examination, including wear testing, microhardness, and microstructure.

3.2.4. *Microstructure and phase examination*

The JEOL (JSM-6010PLUS/LAM Peabody, MA, USA) analytical SEM fitted with EDS was used for examination of microstructure, phases, morphological variations, grain size and other microstructural observations. Elements present within the samples were identified by EDS. Composition and distribution analysis of phases and elements, mainly Ti, Al, Si, Mo and V were done. The electron back-scattered diffraction (EBSD) analysis was implemented using ZEISS Crossbeam 540 (Zeiss International, Oberkochen Germany) FIB-SEM furnished with symmetry EBSD detector. Phases identification and calculation of phase fractions in alloy samples were performed. The phases present in the alloys were characterized via XRD analysis using the PANalytical Empyrean (Malvern Panalytical Ltd, United Kingdom) machine. This approach is centered on studying the scattered beam intensity of X-ray as a function of scattered and incident polarization angle, sample energy or wavelength. This employs a Cu-Kα monochromator as radiation source to study crystallographic structure of samples. Origin 2021, a commercial programme, was utilized to plot the peak graphs. While X-Pert High-Score Plus software was adopted in plotting and documentation of peaks in the plots. Relying on the intensities and peak positions, the background and peak positions were determined; a standard search match was carried out. Using a 0.02° step size, samples were X-rayed throughout a 2θ range of 5° to 100°. Quantifiable analysis of XRD

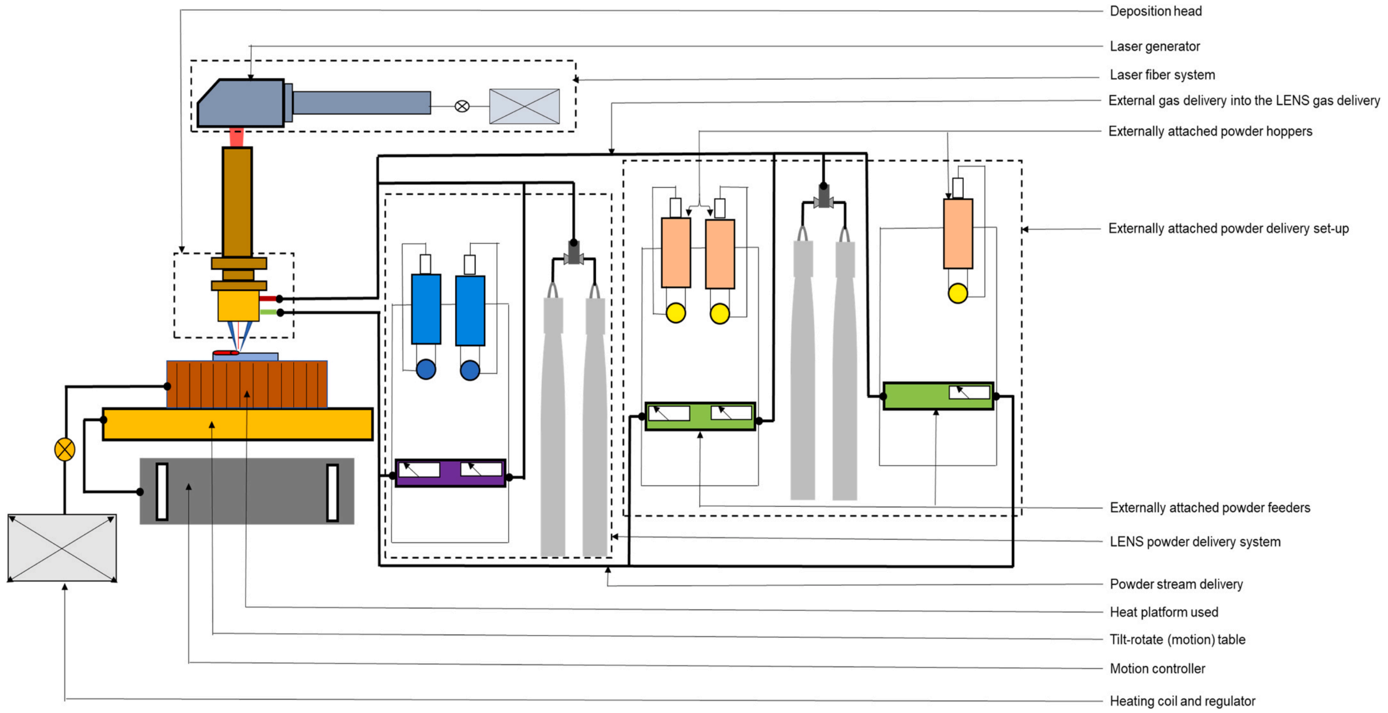

Fig. 2. Schematic Design of the Modified Optomec LENS System.

patterns of the samples were carried out by fitting the patterns of diffraction.

3.2.5. *Microhardness testing*

Hardness testing is an easy and faster method of having some idea about a material's mechanical properties. The hardness of samples was evaluated using Zwick/Roell, ZHVμ (ZwickRoell GmbH, Germany) Vickers' hardness tester. Microhardness testing machine makes use of an optical measuring technique of ASTM E-384 procedure which stipulates a range of light loads utilizing a diamond indenter. A load force of 500gf for 10 seconds dwelling time was used to make a total of thirty (30) indentations each on the samples with 100 μm spacing in between each indent; while average Hv values were reported to represent the microhardness values. A quick approximation of the YS was calculated from microhardness using the empirical relationship between microhardness and YS as shown in Eq. 13 [66,67].

$$\sigma_y = \frac{H_v}{3} \tag{13}$$

where, σ_y is the yield strength (YS) in MPa and Hv in MPa is Hv x 9.81

3.2.6. *Nanoindentation testing*

The nanoindentation testing was performed by means of the Anton-Paar TTX-NHT3 (Anton Paar GmbH, Austria) nanoindentation tester having a 20 nm radius Berkovich indenter tip. The nanoindentation testing machine used for this work at the Surface Engineering Research Laboratory (SERL), Tshwane University of Technology, Pretoria, South Africa is shown in Supplementary Material 5. Fused silica as a sample reference was employed to first calibrate the machine prior to testing all of the samples, using a process akin to that covered by Oliver and Pharr [68]. A 200mN maximum loading force was applied, allowed to hold for 20 seconds, and then released for another 20 seconds. The nanoindentation testing process records the load against displacement (or penetration depth). Supplementary Material 6 shows a representative image of a characteristic nanoindentation test load versus displacement curve. The nanoindentation machine only does the calculation to obtain the indentation hardness (HIT), stiffness (S) and elastic modulus (E*) at each point of indentations. Also, the determination of mechanical properties from the resultant curve is not straightforward. Thereby, the data needs to be converted to indentation stress-indentation strain graphs using numerical analysis, thus, the determination of mechanical properties like YS and ultimate tensile strength (UTS) of alloy samples.

In reality, a user of a nanoindentation instrument does not perform the computation or curve fitting to generate the graphs. The operator only does the calibration of area function for indenter tip $A_c(h_c)$ into the machine's software, and the results (E or E_r and H_c) are consequentially generated as output by the software. Supplementary Material 7 displays the indentation section and labels parameters utilized in the analysis reliant on Oliver and Pharr's [68] work. Thus, throughout the nanoindentation loading progression, true stress and true strain are found using Eqs. 18 and 19, respectively.

$$\sigma = \frac{P}{\pi a^2} = \begin{cases} \dfrac{P}{\pi\left(R^2 - \left(R - \frac{h_t}{2}\right)^2\right)} & \sigma \le \sigma_y \\[2ex] \dfrac{P}{\pi\left(R^2 - \left(R - h_t + \frac{3}{4}\frac{P}{S}\right)^2\right)} & \sigma > \sigma_y \end{cases} \tag{14}$$

$$\varepsilon = \frac{4}{3\pi}\frac{h_t}{a} = \begin{cases} \dfrac{4}{3\pi}\dfrac{h_t}{\sqrt{R^2 - \left(R - \frac{h_t}{2}\right)^2}} & \sigma \le \sigma_y \\[2ex] \dfrac{4}{3\pi}\dfrac{h_t}{\sqrt{R^2 - \left(R - h_t + \frac{3}{4}\frac{P}{S}\right)^2}} & \sigma > \sigma_y \end{cases} \tag{15}$$

The curve fitting approach used in this work uses indentation parameters based on stress-strain properties. Thus, the true stress-true strain graphs from indentation stress-indentation strain curves were fitted into the power law equation. This particular technique is valid for almost all engineering materials. The straight line at the beginning of the graphs is the elastic region with a plastic section observed beyond the yield point. As observed in Supplementary Material 9, during the loading period the three areas of elastic, elastic-plastic and plastic are noticed. The gradient of initial linear section is the elastic modulus, E, in the elastic area. The end of elastic zone gives the yield point (or YS) that signifies the start of the elastic-plastic regime. Also, the UTS is the peak point at the topmost part of the curve just before the stress reduction is observed. It should be noted that this curve (Supplementary Materials 9) could be applied to all types of indenters after producing true stress-true strain graphs based on the nanoindentation results.

3.2.7. *Wear tests*

The investigation of tribology has to do with lubrication, wear and friction taking place on the surface of materials. This is an essential fundamental research area needed for advancing high-performance components. The response of the fabricated alloys to wear was examined by employing Anton-Paar TRB^3 tribometer (Anton Paar GmbH, Austria) using a pin-on-disc based on ASTM G99 and ASTM G133 standard having stainless-steel balls. This is suited for tribology testing because of its wide range of testing parameters. The tribometer systematically measures the results of the friction between the two surfaces with the aid of a friction force sensor and plots the resultant friction data in real-time. For each of the test samples, a sliding distance of 3000 mm was covered in 900 seconds under an applied stress of 20 N. The wear tests were performed at a sliding speed of 0.2 m/min and normal load of 20 N at RT. This method is regarded as sufficiently trustworthy to estimate the functioning of the alloys in terms of tribology.

3.2.8. *Thermogravimetric analyzer (TGA) tests*

The fabricated alloys were studied with the aid of a PerkinElmer thermogravimetric analyzer (TGA 4000; PerkinElmer Inc., USA) used to determine the change in the weight of the samples relative to the unit time with temperature. An inlet gas of N_2 and O_2 with a composition of 79 % and 21 %, respectively, was infused at 20 ml/min. At 50 °C/min heating rate to 900 °C maximum temperature attained for the tests. A built-in accurate weigh balance with a pan inside the chamber during heating monitors the change in weight of the samples at various stages of the experiment up to the maximum temperature. TGA graphs were plotted from the results obtained; this consists of temperature (°C) on the x-axis and mass loss (or gain in mg) on the y-axis. The next section presents and discusses all the findings of this investigation.

4. Results and discussions

4.1. *Simulation results*

In this work, COMSOL Multiphysics was implemented to analysis the influence of processing temperature on temperature profile and stress for TiAl-based alloy. The simulated results serve as the basis for using the heating platform during our experimental work, thus, validates our model. The approach of experiment and modelling carried out was decisive for fabricating better sample structures with limited cracks and defects. Thus, producing TiAl samples with minimal distortions and good component quality.

4.1.1. *Temperature profile during deposition*

The Figs. 3a and 3b presents the transient temperature profile of the rectangular block built at ambient temperature and 800 °C, respectively. The acute rise in temperature depicts the laser interaction when melting the metal powder along build direction; while a drop-in temperature depicts the laser idle time when laser beam is off and the melt pool solidifies during cooling. The peak points show the completion of a particular layer of the build. However, in both cases the maximum temperatures of the succeeding layer are higher than the preceding layers, except at the time, 120 seconds where peak temperature drops slightly less than the preceding layer. This was attributed to the prolonged idle time in switching from building the layers by x-axis to building via y-axis. Although, the cooling rate in both scenarios are similar, the minimum temperature in each case is not the same. This is because both simulations were subjected to similar conditions but the pre-heating temperature makes the build in Fig. 3b experience higher temperatures and stability during the DED processing of the TiAl alloy. The highest temperature recorded for the build process at ambient temperature was about 1100 °C at the 20th layer when building along the y-axis. But the highest temperature recorded for the build process at 800 °C is about 1900°C noticed at the 17th and 18th layer when building along the y-axis.

Generally, when building along the y-axis, the temperature was very high regardless of the processing temperatures. This was ascribed to the shorter length of the build in the y-axis and the re-melting of the first set of layers build along the x-axis. It is understood that the DED process has rapid heating and cooling regime which affects part quality and formation of cracks especially for intermetallic alloys like TiAl. This is influenced by the temperature variations due to inhomogeneous distribution and thermal gradient [69]. It was observed that the average temperature gradually increases all through the build. This demonstrates that the temperature would continuously increase as more layers are added.

4.1.2. *Melt pool*

The fabrication of the rectangular block in stages at different times with a focus on the stability of melt pool region is presented in Fig. 4. The yellowish-white colored portion denotes areas that has higher temperatures than the liquidus temperature TiAl alloy. As observed from

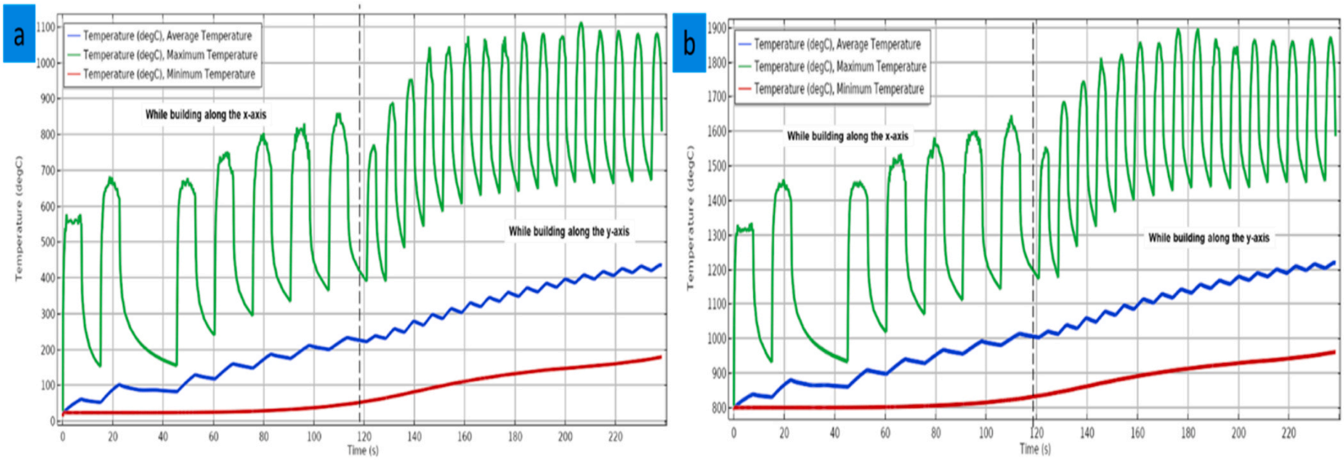

Fig. 3. Temperature History Profile of the Rectangular Block Build at (a) Ambient Temperature; and (b) 800 °C.

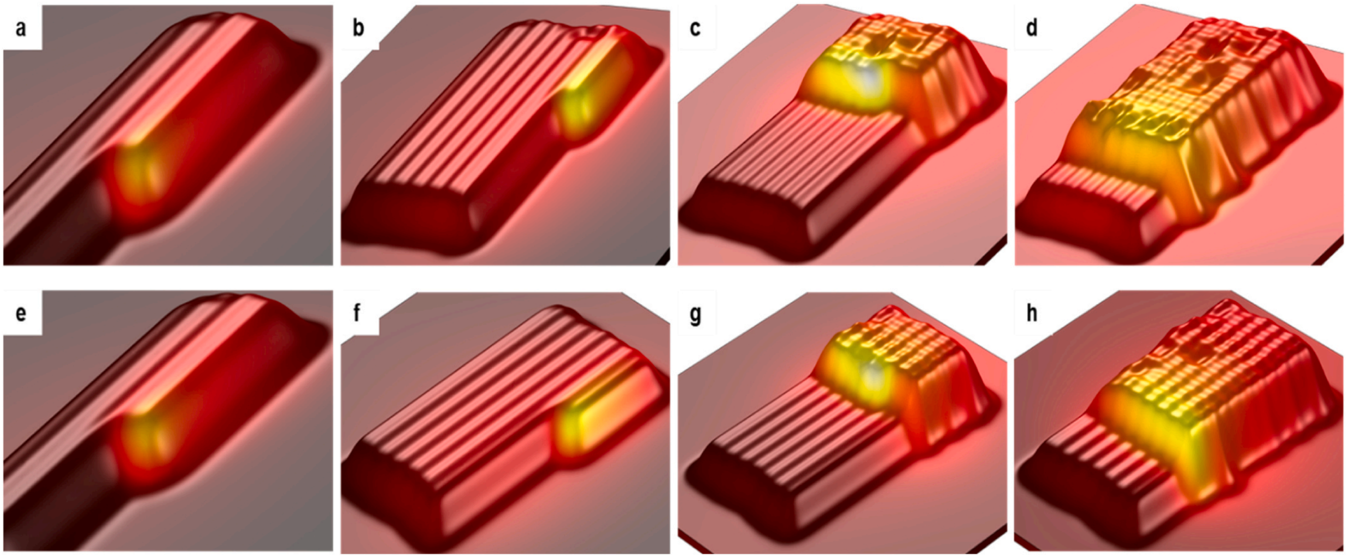

Fig. 4. Showing the Forming of the Rectangular Block Build at Ambient Temperature for (a) 49.6 seconds, (b) 109.1 seconds, (c) 168.6 seconds and (d) 218.2 seconds; the build at 800 °C for (e) 49.6 seconds. (f) 109.1 seconds, (g) 168.6 seconds and (h) 218.3 seconds.

Figs. 4a and 4e, at 49.6 seconds, the melt pool and the build for both cases look very stable and somewhat similar. But at 109.1 seconds (Figs. 4b and 4f), the build processed at ambient temperature (23 °C) starts to get distorted at the edges while the build process at 800 °C was still very stable without any evidence of defects. Furthermore, more distortions were very visible at 168.6 seconds for the build process at 23 °C (Fig. 4c) and the melt pool seems unstable at this point. It was inferred that the distortion would lead to initiation and propagation of cracks. However, build processed at 800 °C (Fig. 4g) still shows good melt pool stability without any apparent defects noticed. But at 218.2 seconds (Figs. 4d and 4h), the build processed at ambient temperature (23 °C) exhibits lots of distortion all over the surface and at the edges while the build process at 800 °C was showed minimal defects on the surface of the build.

Fig. 5 shows the complete model build of the rectangular block build processed at 23 °C and 800 °C. The examination of the builds suggests that processing at 800 °C would produce a part that has a more stable melt pool to achieve good component geometry. However, the measured build height was lesser than our model prediction value. This was attributed to the thermomechanical analysis assumptions made during simulation. It was discovered that scan speed and laser power have considerable impacts on melting pool size, cooling rate and temperature gradient. This has also been reported by Verma, Mandal and Shukla [69], and proposed that laser power ought to be regulated before continuing fabrication with reduced speed of scanning to prevent cracks. The image of the deposited alloy, which was free of cracks, is shown in Fig. 6(a-d). In this work, the use of continuous heating systems lowers cooling rate and, thus, thermal stresses that could build up within the alloy, preventing breaking. Part of the laser energy is absorbed and redirected by the stream of powder particles during the DED process, while another portion is absorbed and reflected by the substrate and/or the layers that were hitherto deposited [54]. The observation reveals by this study indicate that the applied heat during DED process would contributed to the cooling rate by maintaining temperature of the prior deposited layers rather than by simply reduces the energy density; thereby, avoiding cracking that would occur in processing TiAl-based alloys. It is reported in literature that even with enough preheating being provided to achieve low cooling rate, as fresh powders entered the melt pool, It doesn't generate a cooling rate that would lead to the build cracking [54]. Thus, the method of continuous heating adopted in this work drastically lowers the cooling rate of the DED process that can result in cracking.

The heat accumulation brought by continuous energy input also has a significant effect on dimensions of the melt, the pace of cooling, and the evolution of the microstructure, all of which are critical to the mechanical performance of the synthesized material [70]. Lower cooling rates result from higher temperatures caused by heat retention in the formed layer and heating during the fabrication of the next deposits. Newly produced grains typically promote coarsening and diminish the grain boundary densities because slow cooling rates can be linked to slow nucleation. Thus, the proposed model demonstrated its ability to be used for detecting the thermal distribution across the rectangular block

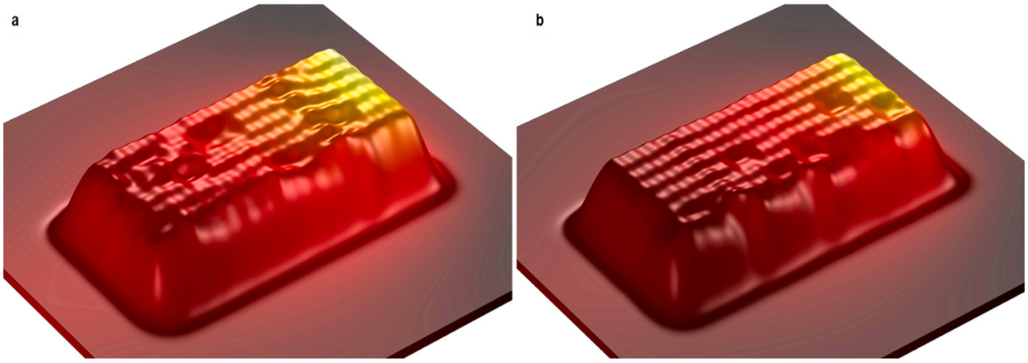

Fig. 5. Complete Build of the Rectangular Block Build at (a) Ambient temperature and (b) 800 °C.

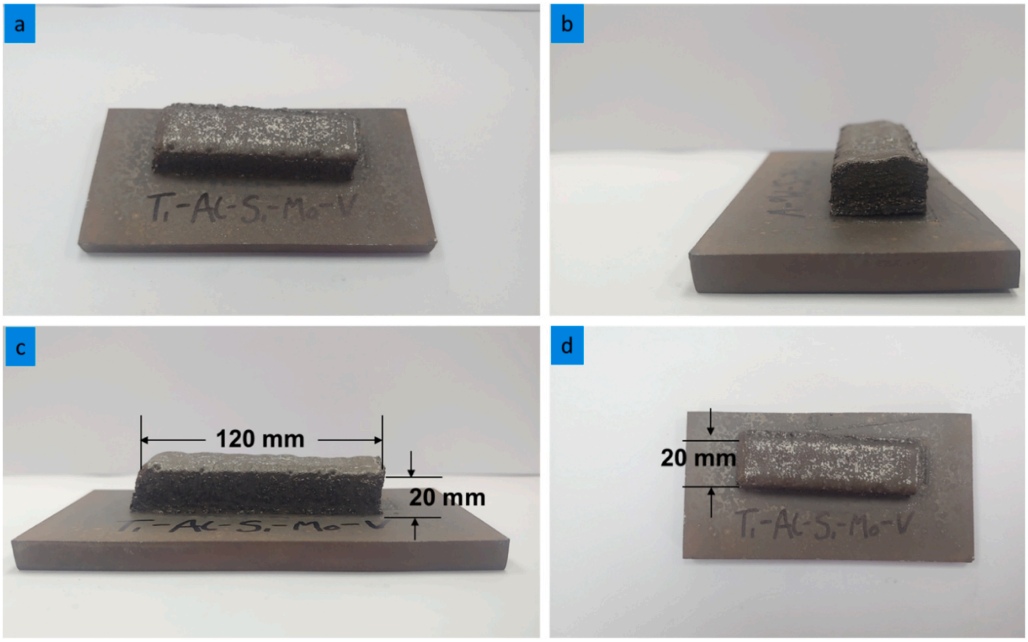

Fig. 6. Image of a Ti-Al-Si-Mo-V Fabricated with the Modified LENS Machine.

and forecasting the effects of processing temperatures and instantaneous temperature build-up. Furthermore, the model disregarded the impact of temperature-dependent fluctuations in thermo-physical properties, which may account for differences between the simulated and real solid/liquid interface. Furthermore, it is known that deep melt pools are produced by high energy densities, whereas shallow melt pools are the result of low energy densities [23,70].

As previously stated, a slight difference in heat flow rate and mass will lead to a huge change in build width, build geometry and build height [18]. This is because mass transfer and heat input perform a key function in DED process. Critical variables that affect heat and mass transfer features include powder feed rate, laser power, scan speed, laser spot size, and the thermal characteristics of the deposited and substrate materials, particularly their melting points. The build width and height are determined by the cross-sectional area and melt pool size, which are determined by these processing parameters [18]. The base plate and/or earlier deposit(s) absorb and reflect some of the residual laser power during the DED process, which is partially absorbed and reflected by the powder particles. The build width and build height of deposited layers will therefore be primarily controlled by the laser energy and powder input volume employed. The comparative reduction in powder catchment and laser irradiation with scan speed will determine the effect on the construction height [18]. In contrast to the one at RT, the heating approach produced greater build-ups because it enhanced the powder catchment during processing. A higher scan speed will result in a lower melt pool temperature and some powder that bounces off the surface after contacting it. This will lower catchment efficiency and lower the build height. The powder spread will be determined by the z-increment, which basically specifies the distance of standoff between the work piece and delivery nozzle. In multilayer deposition, the standoff distance won't change if increment in z is same as the height of layer deposited. Both the laser power density and the powder catchment efficiency will decline with increasing z-increment values. Consequently, the build breadth and size of the melt pool will decrease. A higher laser power will cause the melt pool to become more superheated, the surface tension to drop, and as a result, the construct breadth and height will grow and decrease, respectively. A higher build rate is therefore achievable with the improved DED LENS processing used in this work, as the heating method boosted the efficiency of powder deposition and raised build height. The trapped powder volume in the melt pool will decline with an increase in the powder feed rate; this will reduce melt pool's superheating and lower the build height and overall build.

Powder must be deposited in a regulated way to achieve build with uniform width at consistent build rate for a particular geometry in order to produce components using the DED method. Therefore, for a given set of experimental settings, it is crucial to determine the value range of specific parameter that allow for the stable construction of certain build rate and thickness [18]. The most important finding about evaporation losses is that the chosen laser deposition technique can have a big impact on them [71]. The vaporized mass clearly depends on line offset along with the scanning speed when input energy is constant. During the first passes, the maximum temperature rises, particularly for tiny line offsets when combined with a scanning speed. The heat that remained from earlier scan layers is to blame for this. A certain amount of overlap between neighboring melt clads and between layers created by remelting is usually necessary when fabricating dense objects. Ultimately, the Marangoni effect and surface tension cause the surface to become uneven once the liquid phase solidifies [72]. The laser's energy, the heating platform's energy, and the heat produced by the chemical reaction all contribute to the melting and alloying process. It is imperative to mention that the simulation results are viable where the initial data points are defined since the melting free surface in the computational domain was tracked using the moving mesh technique.

4.1.3. *Surface temperature field*

The surface temperature profile of the rectangular block build at ambient temperature and 800 °C is presented in Figs. 7a and 7b, respectively. The thermal cycle and peak temperatures undergone by each layer has a substantial impact on dimensional accuracy and final produced component's mechanical properties. It was observed that the TiAl deposited at 800 °C had better dimensional accuracy than the build process at 23 °C. Thus, for the purpose of choosing process parameters during the DED processing, quantitative data and comprehension of peak temperatures and thermal cycles of the deposits are essential. In agreement with the heat source model, the highest temperatures were noticed at locations of the greatest heat flux applied [73]. But peak temperature varied with intensity at the surface of TiAl deposited along longitudinal and width paths. The temperature gradient distribution was essentially noticed on the surface as the higher energy density. The material cooling rates during LENS processing were obtained from the

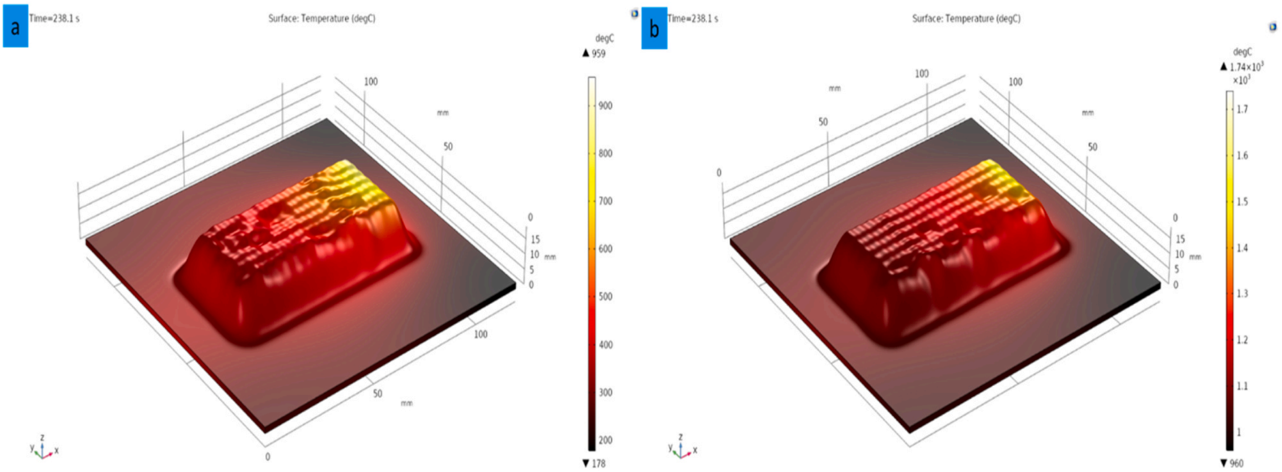

Fig. 7. Surface Temperature Profile of the Complete Rectangular Block Build at (a) Ambient Temperature; and (b) 800 °C.

thermal analysis transient temperature profile on surface melt pool. The TiAl alloy liquidus temperature of 1807°C and solidus temperature of 1719 °C has a close-range which is assumed to be linear in variation with time. It was reported by Balichakra et al. [73], that high cooling rates lead to cracking and fine microstructures with increased microhardness values. Also, the extreme cooling rates can stimulate residual stresses within the melt pool area to create cracks. Consequently, estimating cooling rates when melting permits improved restraint of crack tendency as experienced when processing 800 °C.

4.1.4. *Stress formation*

Figs. 8a and 8b shows the stress deformation contour profile of the rectangular block (in 2D) build at ambient temperature and 800 °C, respectively. It was observed that the maximum Von Mises stress (0.52 GPa or 520 MPa) were similar irrespective of the processing temperatures. However, the lower limit of the deposit build processed at 800 °C was at 1.69 $\times 10^{-4}$ GPa while the deposit build at ambient temperature was 1.39 $\times 10^{-4}$ GPa. This shows that an increase in temperature increases the residual stress within the deposit but does not exceed the UTS of TiAl alloy. Logically, the residual stress obtained should not be more than the YS of the material to avoid cracking [73]. In all AM processes, the repeated heating and longtime of fabrication results in multifaceted strain and stress in the components. This emanates due to contraction and expansion but the component is restrained by the substrate [74]. So, the magnitude of stresses depends on process parameters, material properties, deposition strategy and part geometry. It is ascertained that preheating of the substrate decreases the probabilities of TiAl samples cracking during DED processing. Also, it is deduced that cracking of TiAl samples ensues when building multiple layers of deposits because of the increasing thermal gradients and high rates of cooling increasing residual stresses.

4.2. *Microstructural analysis*

Fig. 9 shows the SEM micrographs of as-built Ti-Al-Si-x(Mo+V) alloy samples fabricated through the modified LENS system; Table 4 presents the compositions of the as-built Ti-Al-Si-x(Mo+V) alloy samples fabricated with the modified LENS system. The as-built microstructures of Ti-Al-Si-x(Mo+V) contains largely α_2/γ lamellae with comparatively small quantity of β_0-phase and ζ-Ti_5Si_3. The quintenary alloys of Ti-Al-Si-x (Mo+V) show lamellar microstructures promoted by the addition of 0.50 g/min and 0.35 g/min of V including the presence of high Al. Both Al and V aid the development of $\alpha_2+\gamma/\gamma$ lamellae thereby reducing the quantity of β_0 formed. As the Mo+V is increased from 0.05 g/min Mo + 0.35 g/min V to 0.05 g/min Mo + 0.35 g/min V, the Si remain virtually the same while the high quantity of V causes a reduction in Al from 47.95 at% to 46.92 at%. It was deduced that increase in the β_0-phase in the 0.05 g/min Mo + 0.50 g/min V alloy was caused by the rise in V from 6.13 at% to 9.35 at%. Moreover, the Al content is sufficient to favor formation of γ-phase needed to promote lamellar formation to achieve good mechanical performance. The small addition of Mo being a very strong β-stabilizer is anticipated to help enhance the mechanical properties. The β-phase tends to cause shrinkage of the α_2/γ grains owing to their superior specific strength, thus, at high quantities would be a detriment to the alloy's mechanical properties and microstructure.

Fig. 10 shows the SEM images of heat-treated Ti-Al-Si-x(Mo+V) alloy

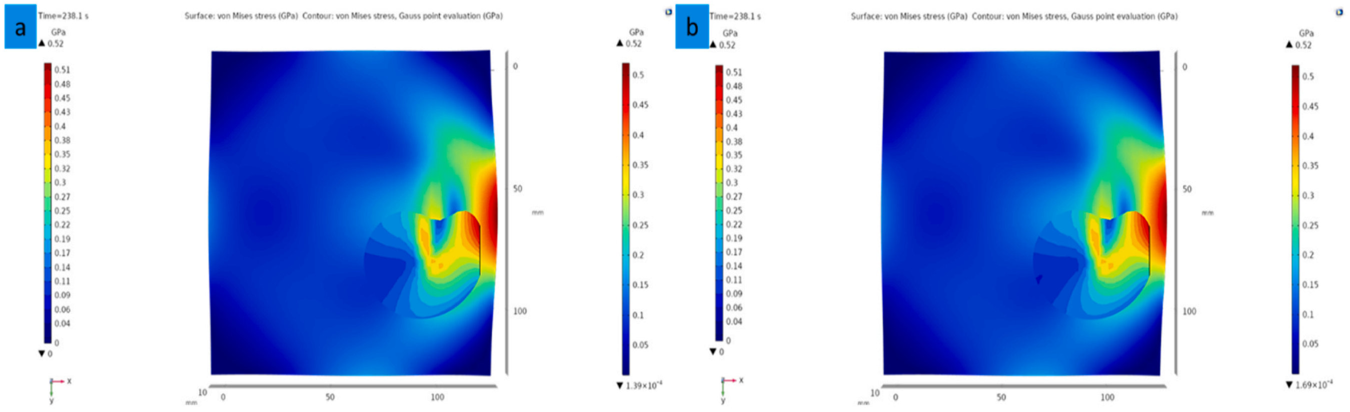

Fig. 8. Stress Deformation Contour Profile of the Rectangular Block (in 2D) Build at (a) Ambient Temperature; and (b) 800 °C.

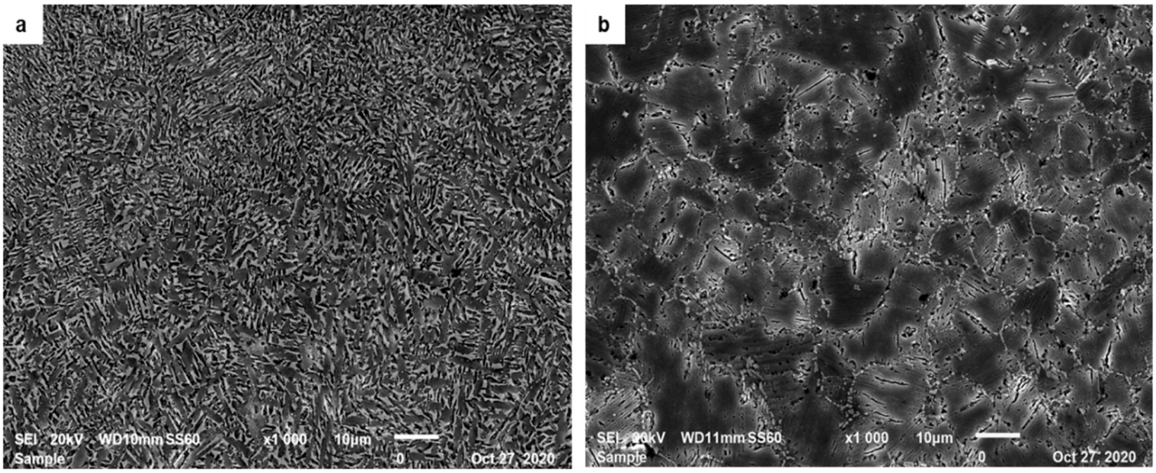

Fig. 9. SEM Images of as-build Ti-Al-Si-x(Mo+V) Sample Processed at (c) 0.05 g/min Mo + 0.50 g/min V, and (d) 0.05 g/min Mo + 0.35 g/min V Fabricated with the Modified LENS Machine.

Table 4
Composition of As-Build Ti-Al-0.025 g/min Si-x(Mo+V) Alloys Fabricated with the Modified LENS Machine.

	Al (at %)	Si (at %)	Ti (at %)	V (at %)	Mo (at %)
0.05 g/min Mo + 0.35 g/min V	47.95	0.93	43.78	6.13	1.21
0.05 g/min Mo + 0.50 g/min V	46.92	1.00	41.51	9.35	1.22

samples fabricated with the modified LENS system; while Table 5 presents the compositions of heat-treated Ti-Al-Si-x(Mo+V) alloy samples fabricated with the modified LENS system. The phases present in heat-treated alloy samples fabricated are α_2+γ/γ, β_0 and ζ phases. The phases identified in all the alloys being developed were all identical but with varying proportions of those phases in the microstructures. It was noticed that the heat treatment technique adopted promotes microstructural refinement because of the presence of Si. This can be easily noticed for all heat-treated samples especially all the 1400 °C/60 mins/FC as compared to 1200 °C/60 mins/FC forming lower quantity of β_0-phase. The heat-treated samples generally had high Al content than their as-built alloys. The composition of Mo in the heat-treated at 1200 °C/60 mins/FC 0.05 g/min Mo + 0.35 g/min V alloy slightly increases while the others remain relatively unchanged with the as-built sample content. Meanwhile, the Al content increases for all heat-treated alloys regardless of the mass flow rate of Mo+V heat treatment temperatures. The Si, Mo and V composition only vary slightly with heat treatment and was relatively unchanged irrespective of Mo+V mass flow rates and heat treatment. The formation of γ is promoted by the Al content thereby restricting β_0 and ζ phases. Likewise, V which is a weak β-stabilizer also contributes to α_2/γ stability in the microstructure. Thus, the ζ-Ti_5Si_3 phase would easily be able to dissolve the β-phase because Mo which is an effective β-stabilizer is present in minor quantities. Consequently, β_0 phase dispersion was achieved due to the occurrence of ζ-Ti_5Si_3 phase.

It was noticed that as-built samples reveal α_2+γ columnar grains of with suspected unmelted Al, β_0-phase and ζ-Ti_5Si_3-phase noticed both at interfaces and within lamellar grains. Al dissolution was noticed to result in the transformation and formation of large-grained lamellar microstructures after heat treatment. The as-built microstructure demonstrates grain disintegration with the lamellae colonies and the grain boundaries interfaces. The grain disintegration appears to reduce after heat treatment but still exist at the interfaces of grain boundaries as noted in Fig. 10. The grain size of as-built quintenary Ti-Al-Si-Mo-V alloy was between 13.467μm to 4.056μm (Fig. 9) while the heat-treated samples' (in Fig. 10) were much bigger with grain sizes up to 100μm for the 1400 °C/60 mins/FC heat-treated sample. This is credited to the heat treatment temperature regime adopted leading to grain growth and lamellar coarsening. The 1200 °C/60 mins/FC heat-treated sample reveals a DP microstructure. But the 1400 °C/60 mins/FC heat-treated sample indicates a fully lamellar (FL) microstructure having precipitates of suspected β_0-phase and ζ-Ti_5Si_3 particles that were anticipated not visibly noticed. The as-built microstructure appears to be inhomogeneous with grains of both coarse and fine irregular lamellar structures. As reported by Hoosain et al. [45], large lamellar colonies of about 250–500μm would be produced when TiAl alloy heat treatment is performed over the α-transus temperatures, thus, leading to FL microstructure as observed in Fig. 10d. It was deduced that heat-treating at 1200 °C tremendously decreases the amount of β-phase within the microstructure. However, heat treating at 1400 °C led to lamellar coarsening and grain growth. The heat treatment temperature was noted to not affect the untransformed γ-grains that looks to be spheriodized [75]. These are positioned within the matrix of the lamellae grains and at grain interfaces. Therefore, it is deduced that α-grain growth was not restricted by γ-grains during heat treatments.

Due to relatively heavy metal like Mo, β phase morphology was brighter as observed from the SEM images. The 1400 °C/60 mins/FC heat-treated sample showed very large lamellar colonies displaying characteristic orientations of lamellae. The grain boundary disintegration of the lamellar grains is believed to have occurred through twinning or recrystallisation of α-grains. Thus, Fig. 10b is understood to display ordered lamellae for the alloy but appeared deformed with discontinuous coarsening close to the α_2-laths. The fine columnar microstructure detected in as-built alloy is different from the NG equiaxed microstructure generally anticipated for most TiAl alloys produce via AM technologies. The suspected phases of β_0 and ζ-Ti_5Si_3 seem to be located at the lamellae interfaces which suggest the limitation of dislocation observed at the interfaces. The transformation kinetics was influenced by the Si through the lamellar spacing refinement of α_2/γ colonies through heat treatment [76]. Thus, ζ-Ti_5Si_3 precipitation via Si addition leads to interface stability and reduction of dislocation movement. However, Si pileup would cause vacancy initiations within the lamellar interface thereby reversing its positive effects of microstructural stability.

The Ti-Al-Si-Mo-V alloy after heat treatment showed a decline in dislocation motion which is expected to result in microstructural stability against thermal degradation and creep improvement [77]. Since strong β-stabilizer like Mo is present, the influence of Mo to stabilize the β_0-phase was reduced for this alloy as Mo was about 1.0 at% of the alloy

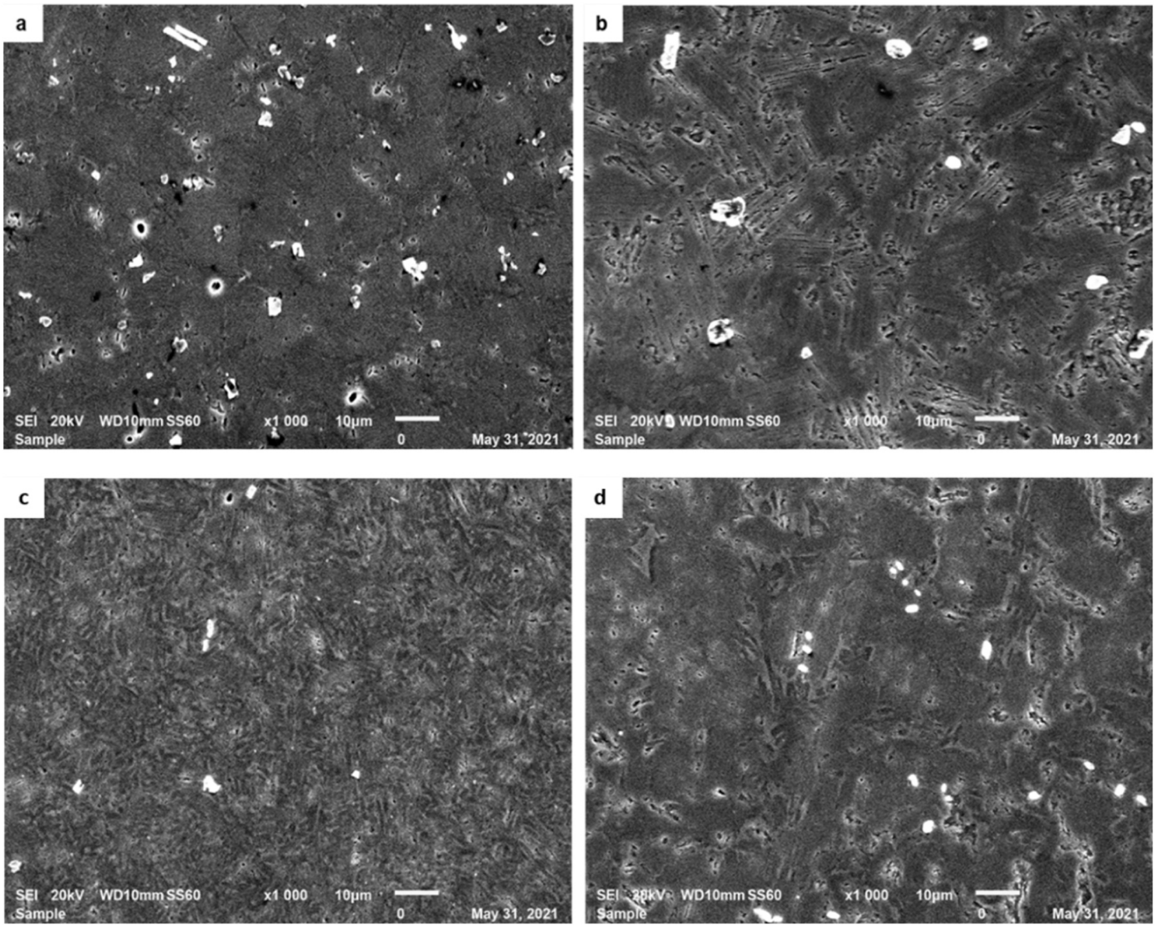

Fig. 10. SEM images of Ti-Al-Si-0.05 g/min Mo + 0.35 g/min V Heat Treated at (a) 1200 °C/60 mins/FC, and (b) 1400 °C/60 mins/FC; and Ti-Al-Si-0.05 g/min Mo + 0.50 g/min V Heat Treated at (c) 1200 °C/60 mins/FC, and (d 1400 °C/60 mins/FC Fabricated with the Modified LENS Machine.

Table 5
Composition of Heat-Treated Ti-Al-0.025 g/min Si-x(Mo+V) Alloys Fabricated on the Heating Platform.

	Heat Treatment Conditions	Al (at %)	Si (at %)	Ti (at %)	V (at %)	Mo (at%)
0.05 g/min Mo + 0.35 g/min V	1200 °C/ 60 mins/FC	49.10	1.18	41.50	6.75	1.47
	1400 °C/ 60 mins/FC	49.33	1.00	42.29	6.27	1.11
0.05 g/min Mo + 0.50 g/min V	1200 °C/ 60 mins/FC	47.12	1.01	40.82	9.84	1.21
	1400 °C/ 60 mins/FC	46.45	0.92	41.72	9.81	1.10

composition. Hence, limiting quantity of β/β_0 phase in the overall alloy. However, the $\gamma+\alpha_2/\gamma$ lamellae colonies were stabilized by V which was about 8.0 at% of the alloy content. It was noticed that γ-phase grew steering coarse lamellar grains formation due to slow cooling during heat treatment and fast growth rate accompanying high-temperature solidification reactions. Moreover, the α-phase was nucleated via peritectic reaction which is expected to lead to the diverse crystallographic orientation of the α-phase [78]. Since, the quintenary Ti-Al-Si-Mo-V alloy contains both β and γ stabilizers, during the phase transformations the α-phase region is expected to have a $\alpha+\beta+\gamma+\zeta$ phase transformation system. Nevertheless, owing to the β-stabilizing nature of Mo, the eutectoid line transforms to a $\beta_0+\alpha+\alpha_2+\gamma+\zeta$ phase region, thus producing two new eutectoid points. A small but vital phase that cannot be pictured via SEM is the ω_0-phase due to its extremely fine nature [64, 79]. This phase has been investigated by many researchers and reported to have been transformed from the $\beta_0(\omega)$ phase and observed within the β_0-phase of lamellar colonies. It is significant for this type of material because the alloys' mechanical characteristics are exceptionally sensitive to the microstructure produced. However, this is beyond the scope of this current study.

A substantial collection of studies has been conducted to examine the impact of minute additions of ternary alloying elements on RT ductility. The main focus of those studies has been on altering the crystal structure of the two principal phases of α_2 and γ. To increase processability, quaternary and ternary alloying additives were used. An alloy that is now in use has a composition that includes both Nb and Cr along with an Al content, ensuring that transformation occurs via peritectic reaction [80]. Si-containing TiAl alloys are promising alloys use in the automotive and aerospace fields at high temperatures [77]. Si is considered as a very good alloying element when enhancing the strength of Ti–Al alloy systems at high temperature, yet its use in TiAl-based alloys is frequently contentious [64]. This is because the ζ-Ti_5Si_3 phase (hcp structure) that was generated serves as a reinforcing phase for the TiAl intermetallic alloy-based reinforcement. Owing to eutectoid production, the formation of silicide is mostly near the interface of α_2/γ lamellar, which increases the creep resistance by adorning γ-(111) planes and preventing dislocation motion [3].

Therefore, it is feasible to increase ductility while maintaining the DP microstructure by adding the proper alloying elements and manipulating the microstructure [80]. For the reason that the corresponding anisotropy of the component phases, TiAl alloys lamellar have weak ductility in part because of their considerable plastic anisotropy [81]. As

TiAl alloy develops towards greater temperatures and enhanced performance, β stabilizers become an essential alloying ingredient. Furthermore, Mo addition enhances the TiAl alloy's oxidation resistance, microstructure stability and RT ductility, while Nb addition increase activation energy of diffusion and negatively impact the alloy hot deformability [21]; V significantly increased TiAl's hot workability as a β phase stabilizer, but it also decreased the metal's resistance to oxidation. Therefore, the ability of Mo and V to stabilize the β phase was considered and this study emphasizes the impact of co-adding Mo and V on mechanical properties and microstructure. Nonetheless, the as-built samples' TiAl microstructure is primarily made up of grains of coarse columnar, which may result in low elongation-to-failure and anisotropic fracture toughness below 700°C [27]. Thereby, rigorously restricts their further advancement which has led researchers to try finding novel approach for processing γ-TiAl alloys. Consequently, the DED LENS modified technology along with the in-situ powder deposition adopted in this work.

Following the heat treatment at 1400 °C, a FL microstructure was formed. The ζ-Ti_5Si_3 phase partially dissolved β_0 phase in the presence of α_2, resulting in observation of both isolated γ grains and a combination of β_0 and ζ-Ti_5Si_3 grains along colony interfaces. It was demonstrated that some of the large lamellar colonies are divided into fine lamellar grains by the β/β_0 phase, which is dispersed at the margins of $\alpha_2+\gamma$ lamellar colonies and inside $\alpha_2+\gamma$ colonies. The coarsened β_0-grain seen at the colony grain boundaries and the black lamellae structures that developed in the lamellae microstructure are recognized as the γ phase [3,32]. The β_0/B2 phase that occupies the lamellar grain boundary remains primarily distributed near the fine γ grains, even if the β_0/B2 phase inside the lamellar colony grows and precipitates thereby dividing the lamellar colony into diverse smaller lamellar clusters. The alloy undergoes structural refinement, coarsening of the grains and change due to the various temperature profiles it encounters during laser printing. Following the heat treatment, the columnar feature vanishes and the microstructure is characterized by FL colonies that are randomly oriented. For all the alloys, it is confirmed that there are small amounts of ζ-Ti_5Si_3 grains along the edges of the α_2/γ colonies. A distinction between the alloys can be seen by comparing the α_2/γ colony. Precipitation is seen in several regions of the alloy's microstructure with respect to the silicide. Heat treatment forms most of the silicide that precipitates in the globular γ phase. The globular γ phase and α_2/γ colonies are the two main boundaries where a little quantity of silicide is generated in the β_0 phase. The majority of the silicide generated at the colony boundary located in the region of the globular γ phase, which is responsible for their precipitation and has a poor solubility for Si. Si enriches the β_0 phase during the $\beta \rightarrow \alpha$ transformation because it is more soluble than the α/α_2 phase in silicide. This creates a force that counteracts the α phase's grain expansion by reducing the grain size owing to solute drag [3]. The coarsening behaviour of α_2/γ colonies is determined by the phases that are present, specifically the β_0 phase near the colony borders, as 1200°C heat treatment temperature falls within the $\alpha+\beta_0+\gamma$ phase field region. Because of Mo's great stabilizing capacity, it is understood that the presence of Mo will reduce V's β phase stabilizing ability [3,21]. Segregation appears to have resulted from the transformation's elimination of β-stabilizing elements into the interface of α_2/γ [78]. Furthermore, degree of segregation becomes more pronounced due to the inclusion of β stabilizing elements, and β_0/B2 phase bands emerge in lamellar boundary or within the interior of lamellar [12]. The discontinuous coarsening of the lamellar γ phase or breakdown of β phase combine to generate the blocky structure linked with the white B2 phase.

In general, the process of heat treatment causes α_2/γ colonies and the γ lamellae themselves to become coarser. Massive α_2, β_0, and γ grains were formed as a result of the lamellar colonies completely granulating after 1 hour of FC and annealing at 1200°C, which is within the $\alpha + \beta/\beta_0 + \gamma$ region (Figs. 10a and 10c). Nonetheless, annealing beyond the γ-solvus temperature would cause the secondary α_2/γ lamellar colonies to develop [57]. At lamellar interface of α_2/γ and γ/γ, γ lamellar plane of {111}, fresh α grains can nucleate and develop into plates of α after the process of heat treatment if heated to α + γ region (1400 °C) from RT. It is deduced that because our annealing temperature falls in the α+β area, the lamellar microstructure was due to eutectoid transformation of α grains [57]. The Blackburn orientation connection, $\{0001\}\alpha_2//\{111\}\gamma$ and $< 1120 > \alpha_2//< 110> \gamma$, between the α_2 and γ phase is obeyed, according to earlier investigations [57,82]. The β_0 phase and lamellar interfaces turn out to be the main alloy microstructure, especially after annealing at 1400℃ for 60 minutes. It is expected that as annealing proceeds, the β_0-phase and γ-phase segments would rise at the expense of the α_2-phase, eventually attaining thermodynamically stable equilibrium [17]. Alongside this, in the α_2/γ-colonies, the γ-lamellae precipitation is progressing in the non-equilibrium α_2-phase. Alternatively, by lengthening the annealing time, minor variations in volume of phases of α_2 and γ as noticed. Furthermore, as seen in Fig. 10, a few twinning induced by annealing are discernible by the γ phase. Additionally, it appears that the realization of numerous α orientation alternatives during the solid-state transformation may result in a significant refinement of the as-built microstructure.

4.3. Phase analysis

The phase identification analysis through EBSD and XRD was performed only on the as-built and 1400 °C/60 mins/FC heat-treated Ti-Al-Si-0.05 g/min Mo + 0.35 g/min V alloy. Fig. 11 shows the EBSD analysis of as-built Ti-Al-Si-0.05 g/min Mo + 0.35 g/min V alloy; while Table 6 presents the phase statistics and grain statistics of the as-built alloy. As observed from the analysis of phase mapping (Figs. 11b and 11c), the EBSD shows the presence of α_2-Ti_3Al, γ-TiAl, α-$TiAl_3$ and confirms the presence of suspected phases of β_0-TiAl and ζ-Ti_5Si_3. The phase was dominated by the γ phase which is 79.97 % volume fraction (Table 6) of phases present in as-built alloy; while α and α_2 phases were 6.69 % and 7.80 % volume fraction of phases present, respectively. The ordered β_0-phase was 1.83 % volume fraction of phases but disordered bcc β phase was not detected. This further proves that Mo stabilizes the β_0 instead of the disordered β phase. Moreover, the amount of β_0 formed was small which was attributed to about 1.0 at% of Mo in the alloy composition. However, volume fraction of ζ-Ti_5Si_3 phase present is 3.34 % which contributes to dissolving some amount of β_0-phase contained in the alloy. The metastable α-$TiAl_3$ detected indicates formation of supersaturated α owing to γ phase being the dominant phase within the microstructure. This is credited to Al content which favors γ-phase formation and the characteristics of V to promote $(\alpha_2+\gamma)/\gamma$ lamellae in the presence of stronger β-stabilizing element like Mo.

Fig. 12 shows the EBSD analysis of Ti-Al-Si-0.05 g/min Mo + 0.35 g/min V alloy heat-treated at 1400 °C/60 mins/FC; while Table 7 presents the phase statistics and grain statistics of the heat-treated alloy. As observed from the phase map analysis (Figs. 12b and 12c), the EBSD shows the presence of α_2-Ti_3Al, γ-TiAl, α-$TiAl_3$ and confirms the presence of suspected phases of β_0-TiAl and ζ-Ti_5Si_3. The dominate of the γ-phase has been reduced due to heat treatment but the volume fraction is 53.22 % (Table 8) of the phase presence after heat treatment. This was suggested to be attributed to phase transformation reactions occurring above the α-transus temperature and Al evaporation at 1400 °C for a prolonged amount of time. However, the α and α_2 phase volume fractions increase to 23.45 % and 15.97 %, respectively. The amount of the ordered β_0 phase volume fraction was also decreased to 1.21 % of the phase while the disordered bcc β phase could not still be detected. Thus, confirming Mo propensity to stabilize the β_0 instead of the disordered β phase. Conversely, the ζ-Ti_5Si_3 phase volume fraction increases to 6.14 % which was almost double the amount present in the as-built sample. The increased amount of the ζ-Ti_5Si_3 phase is ascribed to precipitation of more ζ-Ti_5Si_3 phases that dissolves some portion of the β_0-phase in the present in the α-phases that promote ζ-Ti_5Si_3 phase formation. The metastable α-$TiAl_3$ was still detected at the $(\alpha_2+\gamma)/\gamma$

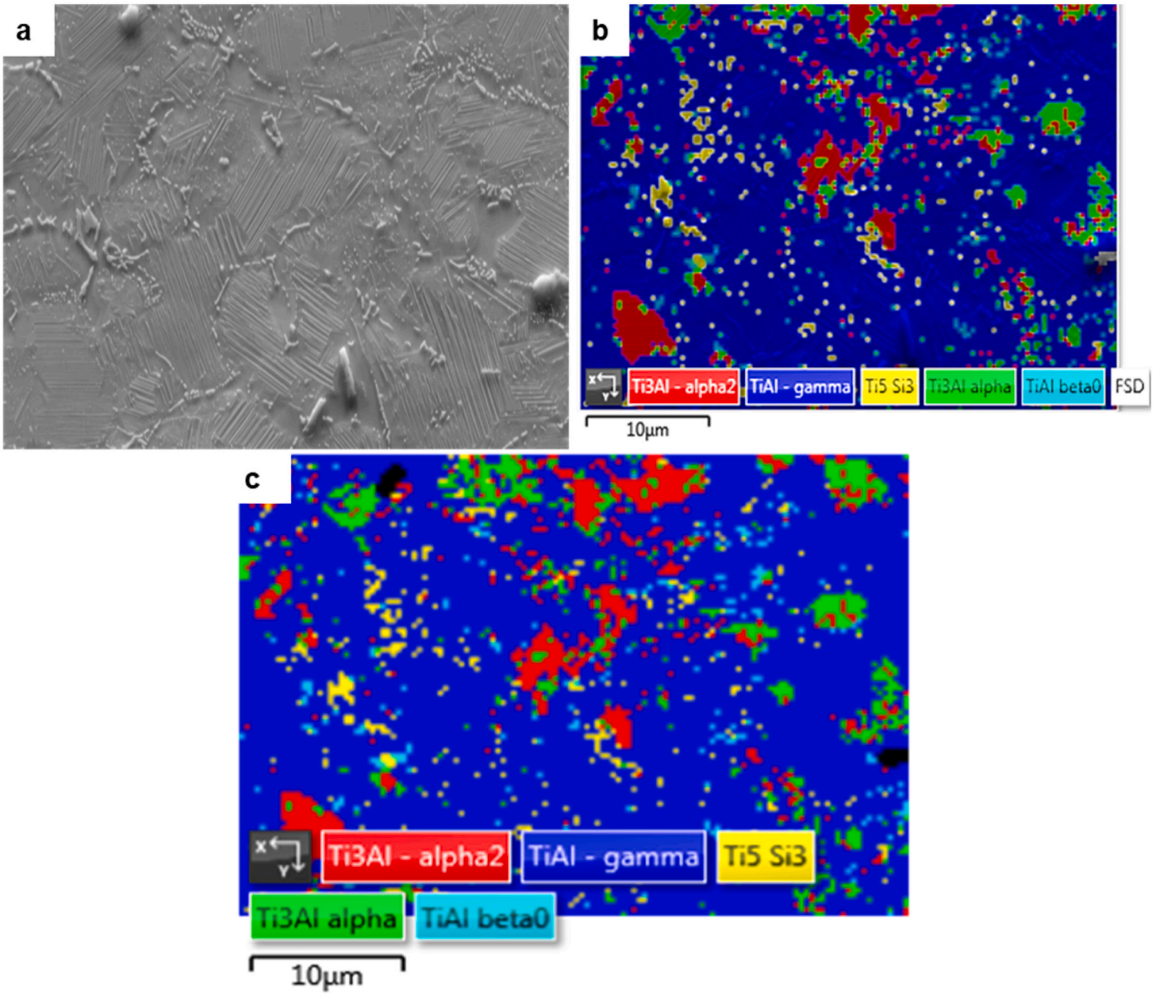

Fig. 11. EBSD Analysis of As-Built Ti-Al-Si-0.05 g/min Mo + 0.35 g/min V Alloy Showing (a) FSD Image, (b) EDS Layered Image, and (c) Phase Mapping.

Table 6
Phase Statistics and Grain Statistics of As-Built Ti-Al-Si-0.05 g/min Mo + 0.35 g/min V Alloy.

Phase	**Fraction (%)**	**Count**	**Mean BC**	**Mean MAD**
α_2-Ti$_3$Al	7.80	959	169.64	0.95
γ-TiAl	79.97	9827	185.20	0.73
ζ-Ti$_5$Si$_3$	3.34	410	179.55	0.79
α-Ti$_3$Al	6.69	822	168.05	1.01
β-TiAl	0.00	0	0.00	0.00
β_o-TiAl	1.83	225	186.08	0.77
Zero Solutions	0.37	45	88.89	-
Measurements	**Minimum**	**Maximum**	**Mean**	**Standard Deviation**
Area (µm^2)	1.18	49.58	4.48	6.61
Aspect Ratio	1.12	4.32	1.72	0.43
Breath (µm)	0.69	7.73	2.07	1.18
ECD (µm)	1.23	7.95	2.10	1.13
GOS (°)	0.12	1.94	0.53	0.27
Length (µm)	1.54	14.18	3.48	2.05
MOS (°)	0.21	4.00	1.27	0.72
Perimeter (µm)	3.80	78.53	10.97	10.07
Slope (°)	5.63	168.75	92.67	47.73

lamellae colonies.

Based on the FSD image in Fig. 12a, the microstructure after heat treatments could be said to be homogenous when compared to the as-built microstructure. Also, the heat-treated sample exhibited refined microstructural effects which display almost uniform orientation distribution of γ lamellae and α/α_2-phase that were nucleated from the γ-phase. The refining of the lamellae was achieved through combined effects of dislocations motions, ζ-Ti$_5$Si$_3$ particles and α_2-Ti$_3$Al grains. It was reported in the works of Schwaighofer et al. [83] and Mathabathe et al. [84], that Mo addition to TiAl alloys leads to microstructural grain refinement with improved high-temperature deformability owing to metastable B2 phase stabilization. The β/β_0-phase volume fraction was decreased via heat treatment because Mo strongly favors β_0-phase formation which could hinder the mechanical characteristics of the alloy.

Fig. 13 displays EBSD analysis within a grain boundary region of the Ti-Al-Si-0.05 g/min Mo + 0.35 g/min V alloy heat-treated at 1400 °C/60 mins/FC while the phase statistics are presented in Table 8. The interface shows that the α and ζ-Ti$_5$Si$_3$ were precipitated within the α_2-phase sites but the β_0 was scarcely observed. This confirms that a certain amount of the β_0-phase was dissolved by ζ-Ti$_5$Si$_3$ within the α_2-phase which aids nucleation site for precipitation of phases in the alloy. The volume fraction of β_o phase at the grain boundary is lesser (1.19 %), even though the α_2-phase volume fraction was higher in this section (29.12 %). The β_0-phase in this situation was reduced through the growth of γ grain from γ-laths within colonies of the lamellae. The initiation of γ coarsening within the lamellae without nucleation was propelled by structural and compositional stabilization of the metastable B2 β-phase structure [85]. The substitution of Al by Mo causes a slight decrease in lattice parameter of β_o but this phase is not mechanically stable except Mo substitutes up to 4 at% Al. When the β-phase becomes stable it limits the coarsening of α-grains by encircling α, therefore, restraining the grain boundaries mobility [76]. From literatures, it is

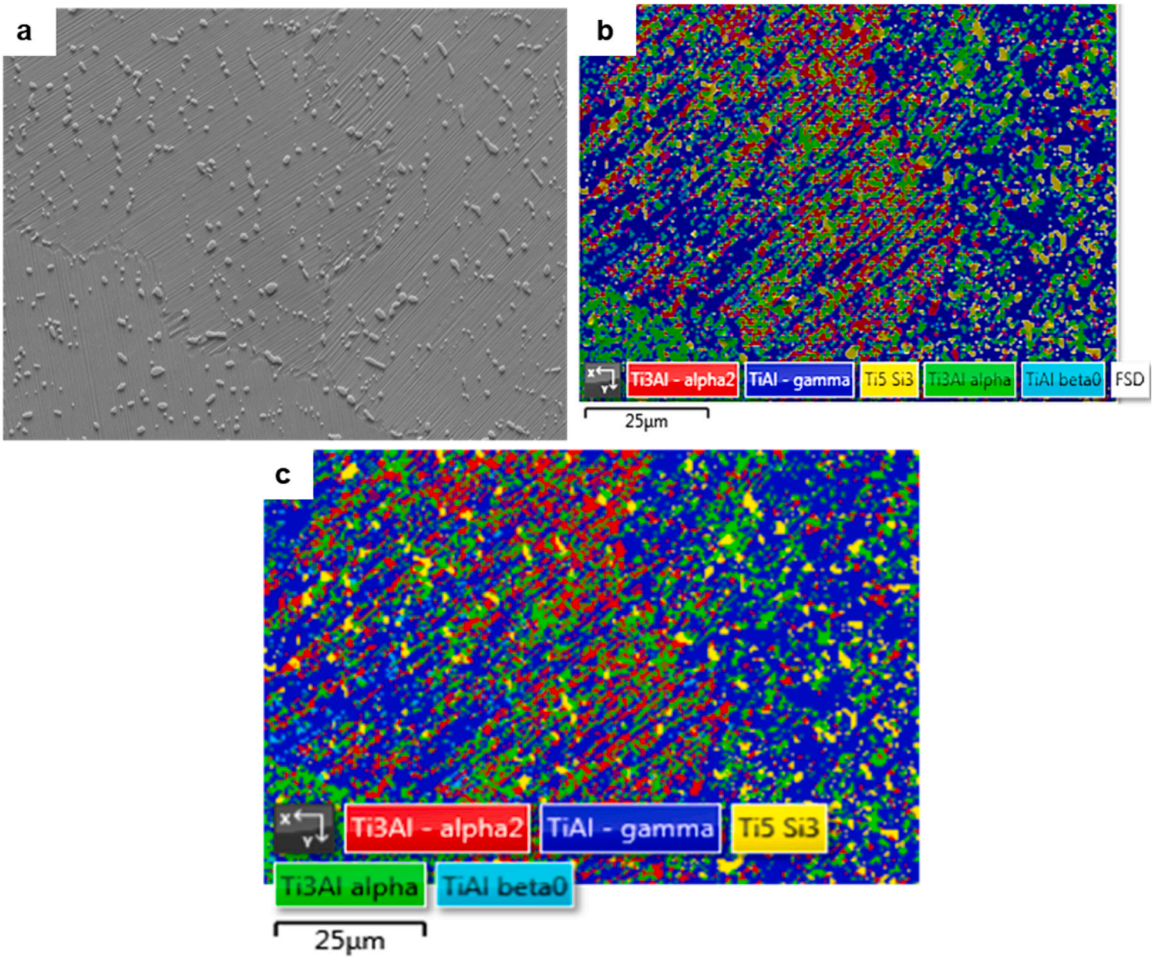

Fig. 12. EBSD Analysis of Ti-Al-Si-0.05 g/min Mo + 0.35 g/min V Alloy Heat Treated at 1400 °C/60 mins/FC Showing (a) FSD Image, (b) EDS Layered Image, and (c) Phase Mapping.

Table 7
Phase Statistics and Grain Statistics of Ti-Al-Si-0.05 g/min Mo + 0.35 g/min V Alloy Heat Treated at 1400 °C/60 mins/FC.

Phase	Fraction (%)	Count	Mean BC	Mean MAD
α_2-Ti$_3$Al	15.97	5796	122.37	0.89
γ-TiAl	53.22	19319	136.48	0.74
ζ-Ti$_5$Si$_3$	6.14	2230	134.41	0.69
α-Ti$_3$Al	23.45	8514	132.85	0.88
β-TiAl	0.00	0	0.00	0.00
β_o-TiAl	1.21	441	127.85	0.87
Zero Solutions	0.00	0	0.00	-
Measurements	**Minimum**	**Maximum**	**Mean**	**Standard Deviation**
Area (μm^2)	2.50	133.50	6.20	9.70
Aspect Ratio	1.09	4.69	1.85	0.51
Breath (μm)	1.00	15.08	2.47	1.24
ECD (μm)	1.78	13.04	2.55	1.18
GOS (^{o})	0.12	2.14	0.52	0.17
Length (μm)	2.24	33.90	4.56	2.97
MOS (^{o})	0.16	4.24	1.06	0.44
Perimeter (μm)	5.53	211.37	13.70	15.74
Slope (^{o})	8.44	168.75	71.54	43.72

understood that the alloying elements addition like W, Ta, Nb and Mo moves the boundary of $\alpha_2+\gamma/\gamma$ towards the Al area but Mn, Cr and V cause a shift to the Ti region.

The avoidance of γ-grains recrystallization can be achieved with the α_2-laths. In the as-built state α_2 volume fraction is 7.80 % which led to substantial lamellae thinning. The increase in volume fraction to 15.97 % leads to a corresponding decrease in the amount of γ-γ interfaces due to extensive dissolution and transformation of two adjacent γ-laths. The presence of coarse ζ-Ti$_5$Si$_3$ particles suggests liquid state transformation in the precipitation of the phase which would

Table 8
Phase Statistics and Grain statistics of the Selected Grain Boundary Area of Ti-Al-Si-0.08 g/min Mo + 0.35 g/min V Alloy Heat Treated at 1400 °C/60 mins/FC.

Phase	Fraction (%)	Count	Mean BC	Mean MAD
α_2-Ti$_3$Al	29.12	3513	142.14	0.70
γ-TiAl	58.24	7027	168.91	0.72
ζ-Ti$_5$Si$_3$	3.83	462	127.36	0.61
α-Ti$_3$Al	7.62	919	161.82	0.86
β-TiAl	0.00	0	0.00	0.00
β_o-TiAl	1.19	144	172.24	0.77
Zero Solutions	0.00	0	0.00	-
Measurements	**Minimum**	**Maximum**	**Mean**	**Standard Deviation**
Area (μm^2)	1.19	253.29	8.64	23.83
Aspect Ratio	1.15	6.56	2.30	0.98
Breath (μm)	0.69	12.47	2.13	1.53
ECD (μm)	1.23	17.96	2.60	2.06
GOS (^{o})	0.15	2.12	0.51	0.28
Length (μm)	1.72	44.53	5.08	5.21
MOS (^{o})	0.27	3.66	1.29	0.69
Perimeter (μm)	4.00	245.46	15.40	24.15
Slope (^{o})	4.22	168.75	64.67	53.05

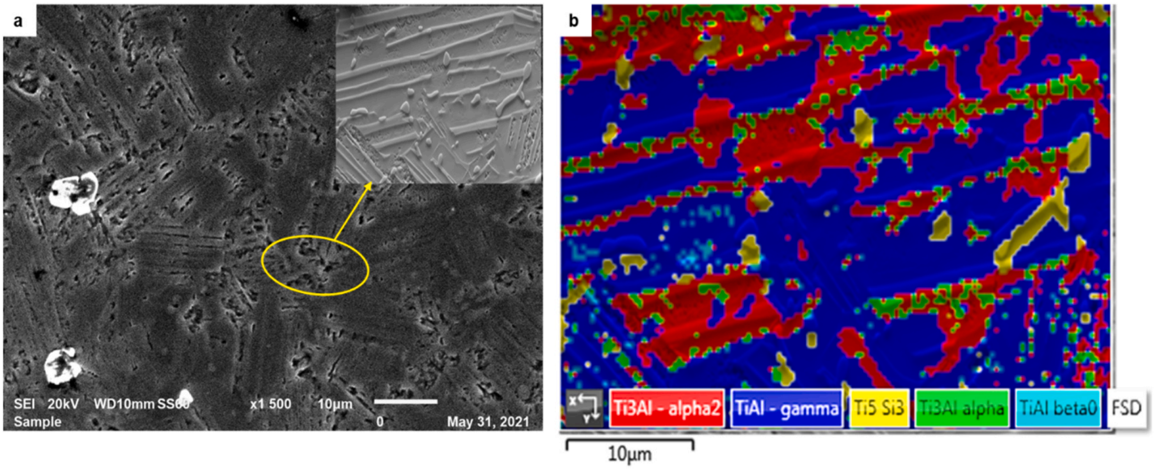

Fig. 13. Showing Grain Boundary Area of Ti-Al-Si-0.08 g/min Mo + 0.35 g/min V Alloy Heat Treated at 1400 °C/60 mins/FC (a) SEM Image with Inset of FSD Image, and (b) Phase Mapping of the Selected Area.

subsequently diminish the tensile properties of the alloy [84]. Si promotes α_2-laths dissolution invariably increasing γ-phase recrystallization. This is attributed to the stronger ability of Si to create vacant sites in the alloy matrix. It was deduced that from the work of Klein et al. [77], that interfacial precipitation arose in the alloy via $\alpha_2 \rightarrow \gamma + \zeta$ eutectoid reaction. However, ζ-Ti_5Si_3 nucleation is heterogeneous within the γ-lath which characteristically ensues at dislocation sites. Thus, indicates that ζ-Ti_5Si_3 particles favorably precipitate at γ-laths

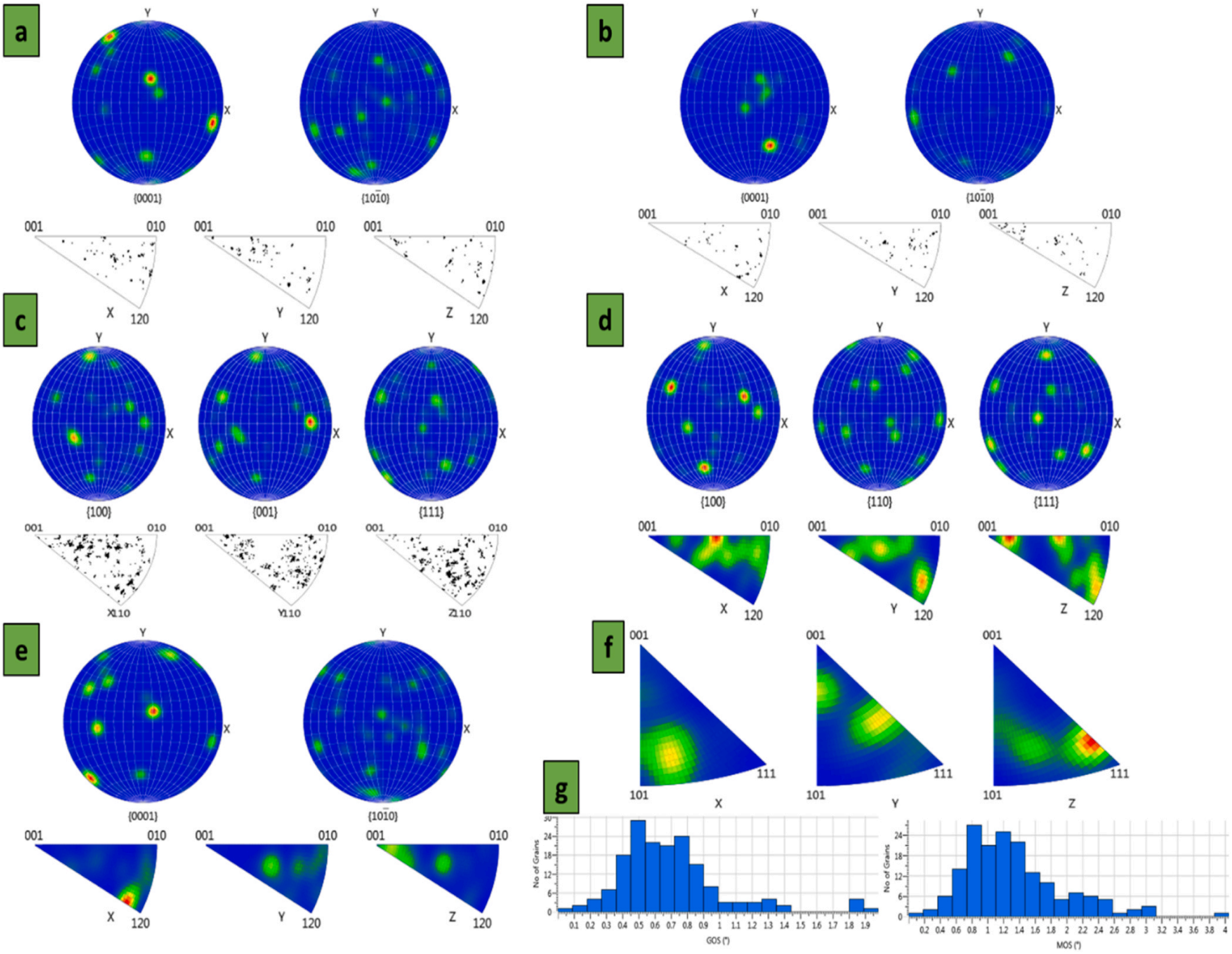

Fig. 14. EBSD Analysis of Ti-Al-Si-0.05 g/min Mo + 0.35 g/min V Alloy Showing Inverse pole figure (IPF) and phase orientation of (a) α_2-Ti_3Al, (b) ζ-Ti_5Si_3, (c) γ-TiAl, (d) β-TiAl, (e) α-$TiAl_3$; (f) overall IPF; and (g) the GOS and MOS of the phases.

lamellae stacking faults [86].

So as to study the phase composition of the samples, EBSD measurements are carried out. The Ti-Al-Si-0.08 g/min Mo + 0.35 g/min V alloy data are summarized in Figs. 14a-g and 15a-g, respectively. As a result, the phase analysis result that is shown is really for qualitative remarks. The as-built and heat-treated samples' phase maps and inverse pole figures (IPF) maps, as well as the phases MOS (maximum orientation spread) and GOS (grain orientation spread), are displayed in the Figures. The average degree of misorientation within grains is displayed on the GOS map. While grains traversed by low GOS holds an even strain distribution, those with large GOS values exhibit significant high dislocation density and crystal lattice deformation. While the MOS (Maximum Orientation Spread) determines the maximum deviation angle relative to the average crystallographic orientation of all pixels within a grain. Furthermore, the as-built alloy consists of α-$TiAl_3$, ζ-Ti_5Si_3, γ-TiAl, β_0-TiAl and α_2-Ti_3Al phases, as signified in the EBSD phase map (Fig. 11). Due to the DED alloy production method maintains a heating temperature of 800 °C, the phases coexist. Fig. 14 displays the pole figures for each phase. α_2 has a strong texture, with its (0001) almost perpendicular to build direction, whereas γ has a weak texture. The GOS map in Fig. 14g, on the other hand, shows that the lamellar colonies have the highest GOS value, while the HAGBs-dominated γ + B2/β grain locations often have the lowest GOS value [87]. A few coarse γ grains also show a moderate GOS value. Furthermore, substantially lower GOS values are found in the relatively straight γ-lamellae and γ grains region inside lamellar structures. But, in comparison to the heat-treated sample (Fig. 15g), annealing led to grain coarsening. Stated differently, as noticed in the microstructure shown in Fig. 10b, a substantial lamellae fraction is almost perpendicular to build direction of the structure. Given that lamellae interface is parallel to $(0001)\alpha_2$ and that the creation of γ laths from α/α_2 sticks to the Blackburn-orientation connection, there is an intense connection among this preference coordination and texture of α/α_2 [24].

The lamellae's preferred orientation suggests that heat treatment in the single a phase zone does not impair the α/α_2 texture. Grain size also has an impact on the texture strength [32]. One plane {111} shared by the twin-related γ-lamellae, as indicated by {111} the phase pole figures in Figs. 14f and 15f. A change in orientation from one of a crystal's symmetrically equivalent coordinate systems to another crystal's equivalent coordinate system is referred to as a misorientation among two comparable crystal structures [88]. It is conventional to select the axis of rotation with the least misorientation angle among all symmetrically equivalent rotations. The lath resulting from misfit dislocation-induced microstructural changes and ledge development is depicted in Fig. 13a by the highlighted circle at the γ/γ interface. Evidently, the comparatively finer grains in this current alloy are a result of the reinforcing components and the mutual strengthening action of the α_2, ζ-Ti_5Si_3, and β_0 phases, despite annealing at a high temperature of 1400°C. The presence of β_0 phase at RT in the current as-built TiAl alloy is explained by isolation of β stabilizing elements at grain

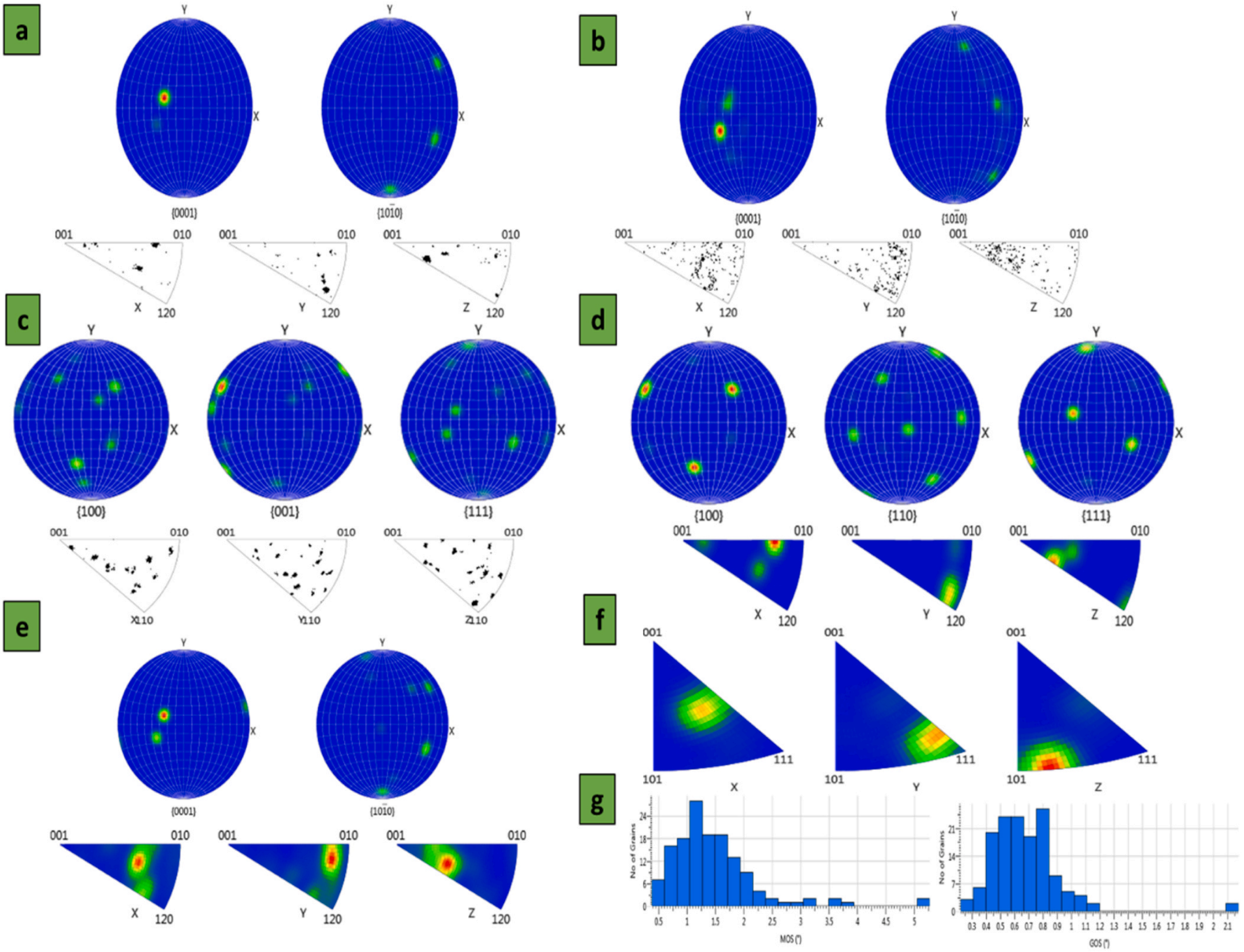

Fig. 15. EBSD Analysis of Ti-Al-Si-0.05 g/min Mo + 0.35 g/min V Alloy Heat-treated at 1400 °C/60 mins/FC Showing Inverse pole figure (IPF) and phase orientation of (a) α_2-Ti_3Al, (b) ζ-Ti_5Si_3, (c) γ-TiAl, (d) β-TiAl, (e) α-$TiAl_3$; (f) overall IPF; and (g) the GOS and MOS of the phases.

boundaries. As a result, annealing at 1400°C for one hour can finish the $\beta \rightarrow \alpha$ transformation, lowering the β_0 phase at ambient temperature.

The annealing process produces coarser microstructures with main constituents of supersaturated α_2, γ, and β_0 as compared to the as-built microstructure. According to the EBSD analysis, heat treatment caused the alignments of the β phase to concentrate along symmetry folds of the {110}, a conventional projection for a cubic system (Fig. 15). enhanced dislocation densities following heat treatment were a clear indicator that more dislocation glide systems had been activated as a result of the enhanced symmetry in crystal orientations [2]. The intricacy of the crystal structure in α_2 phase results in a highly restricted dislocation motion. Higher tetragonal orientations following heat treatment enable dislocations to move along α_2/γ contacts [2]. Heat treatment produced microstructures with a more uniform distribution of crystal orientations, as seen by the decrease in the amount of crystal orientations found in the pole figures following heat treatment. This is obvious in the inverse polar representations that comprises grains appearing more consistent. Moreover, heat treatment resulted in an increase in texture in α_2 orientations but a decrease in texture measures of orientations for the tetragonal γ and cubic β.

In general, FC can efficiently remove residual stress with coarse microstructures and is disposed to achieving α_2/γ lamellar colony equilibrium [57]. The formation of lamellar colonies by eutectoid reaction was aided by slow cooling. Although more α_2 phase was generated as component of the lamellar microstructure showing a drop in β_0 fraction after heat treatment, the EBSD data demonstrate that γ phase is still dominant within the microstructure. First, as usually seen in γ-TiAl alloys during stabilization, the hitherto α_2 supersaturated grains change into lamellar colonies of α_2/γ, consequently, the development of γ lath precipitates ($\alpha_2 \rightarrow \alpha_2/\gamma$) [11]. With regards to performance at high temperatures, Figs. 9a and 9b demonstrate that the microstructural colonies are comprised of alternate ultrafine α_2/γ lamellae that is highly encouraging. However, the ζ-Ti_5Si_3 breaks down some of the β_0 phases, which reduces the overall quantity of β_0 phase and applicable β_0 size in the ensuing microstructure.

While adding V, it does not alter the phase form, it does raise the value of the peak for certain orientations, like (111)γ phase, suggesting that microstructure orientation enhancement has a major impact on the amount of grains having this orientation [12]. More β phases, some of which coarsening of the lamellar structure or the generate γ phases through $\beta \rightarrow \gamma$ transition, find it more difficult to undergo complete transformation through solid phase transformation in the presence of V. Moreover, the same lamellar colony is divided by the banded B2 phase. Beyond and beside the banded B2 phase, several lamellae colonies coarsely merge along the original direction to generate the blocky γ phase. Conversely, Mo and V stabilize the β phase, which is subsequently pushed to the α phase boundary with a different orientation and alienated along the interfaces, hindering the formation of Burgers α grains. The main solid at this composition formed as the disordered β-phase, based on the binary phase diagram of Ti-Al these alloying elements stabilizes β-phase. Following that the primary β phase gave rise to α phase, which followed the Burgers orientation relationship (BOR), i.e., $\{0001\}\alpha || \{110\}\beta$ and $\alpha || \beta$ [89]. According to Klein et al. [90], a higher Mo content stopped the ω_0 nucleation. The XRD patterns and the EBSD data correspond fairly well. The distribution of the discovered β_0 phase is primarily found around the interface. It is worth mentioning that the minuscule β_0 phase found in the colonies of lamellar is present, along with minuscule α_2 lamellae.

Fig. 16 confirms the XRD pattern of phases displayed in the microstructure. Fig. 16 presents the XRD pattern of the Ti-Al-Si-0.05 g/min Mo + 0.35 g/min V fabricated via the modified LENS machine. The XRD results show a pattern with several peaks α_2-Ti_3Al and γ-TiAl with few minor peaks of β_0-TiAl and ζ-Ti_5Si_3 were detected. The β_0-phase was not noticeable for the as-built sample but the 1400 °C/60 mins/FC samples display more visibly and new XRD peaks which is an indication that phase transformation occurred during the heat treatment. Studies about interactions of elemental powder produce metastable phases such as $TiAl_3$ and $TiAl_2$ owing to an occurrence known as Kirkendall porosity [91]. This could lead to β phase formation that is disadvantageous to the alloy's high temperatures mechanical properties. The appearance of high peaks of $\alpha_2+\gamma$ at 2θ between 40° to 45° shows the transformation of lamellar solid solution. The peaks of $\alpha_2+\gamma$ for the heat-treated sample was higher indication more lamellar formation.

However, twinning occurred in both as-built and the heat-treated sample between 2θ equals 40° to 55° but the twinning was less obvious for heat-treated samples. This is indicative of stress relaxation in heat-treated samples. XRD sensed a relational rise in γ-phase peak intensities while twin γ peaks and α_2 peaks were dispersed somewhat reduce. According to Appel, Paul and Oering [62], a rise in Al content decreases stacking fault energy. Since there was a reduction in Al content it can be interpreted that the stacking fault energy for our alloy increases. This further explains the dilation of grain interfaces noticed in

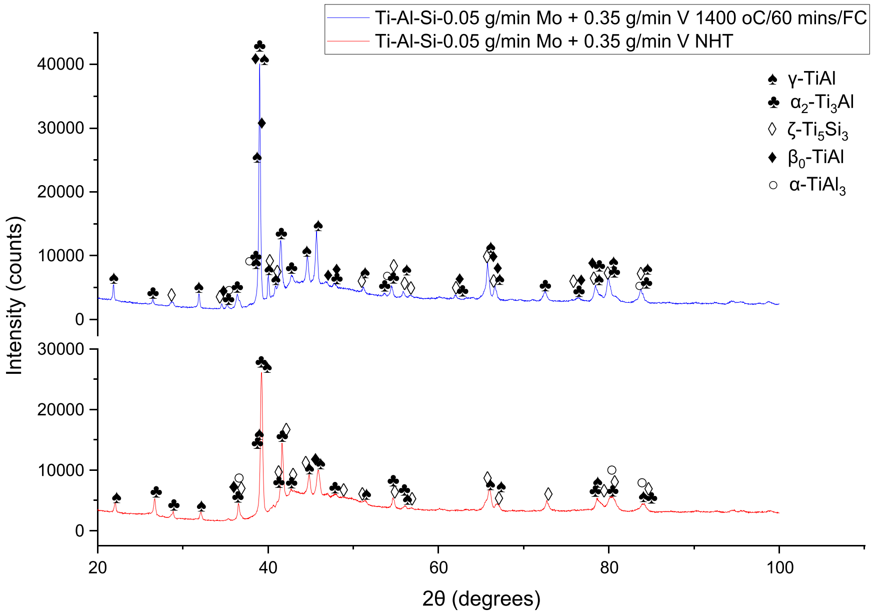

Fig. 16. XRD Analysis of Ti-Al-Si-0.08 g/min Mo + 0.35 g/min V Alloy.

the SEM micrograph of 1400 °C/60 mins/FC heat-treated sample. It is worth mentioning that slip motions in TiAl-based alloys vary depending on Al content, thus, influencing the deformation and twinning. This shows that heat-treated samples would display little or no twinning because of reduced Al content. Moreover, materials that induce twinning possess improve resistance to impact and high formability [45].

The as-built alloy XRD spectrum with respect to HT, indicates that the predominant phases are γ and α_2, as indicated by the high intensity peaks around 39.1° 2θ values. The as-built samples possess higher amounts of α_2 phase prior to depletion after HT. After heat treatment, this peak's strength had somewhat dropped. This indicates that following HT, a portion of the unstable αphases decomposed to create stable phases [7]. The major diffractions peaks of as built TiAl were indicated as: 39.18857°, 41.6417°, 44.8137°, 45.8808°, 54.7854°, 65.9645° and 80.1465° with distance of the inter-planar being 2.29711 Å, 2.16713 Å, 2.02082 Å, 1.97627 Å, 1.67425 Å, 1.41500 Å and 1.19655 Å, respectively. Post annealing HT at 1400 °C, the peaks of diffraction were noticed at: 38.7752°, 39.7971°, 41.2613°, 44.3593°, 45.4406° and 65.3932° with distance of inter-planar being 2.32048 Å, 2.06322 Å, 2.18622 Å, 2.04046 Å, 1.99438 Å and 1.42598 Å, respectively. Planar defects (stacking and twinning) caused the XRD peaks to alter the width (broadening), emergence or disappearance of intensity drop, peak shifts, peaks and rise in noise, according to Hoosain et al. [45]. It is noteworthy to highlight from the above data that HT caused the γ-phase to vanish at around 42° (2θ), the peak shift to occur beyond 70° (2θ), the α_2 phase to max expand at 67.2°, and the intensity to drop with the development of a new phase. This is a sign of Ti-Al alloy twinning and demonstrates how planar flaws are impacted by annealing temperature [7].

Atomic rearrangement is typically indicated by a shift in the crystal's structure and a decrease in peak intensity. Based on to EBSD analysis, there were more prominent γ phase precipitates following HT, whereas the as-built sample appeared to be an alloy rich in α_2. Reasonable toughness, formability, strength, good corrosion resistance, moderate high temperature properties and creep resistance are known characteristics of the α_2 phase. Additionally, it is identified that α_2 phases have restricted slip motions upon deformation, making heat treatment a valuable method of improving TiAl's mechanical properties. Fig. 16 illustrates the existence of dislocations and stacking faults in α_2/γ laths of as-built alloy sample. With respect to high-temperature applications, γ-phase of TiAl-based alloys has desirable characteristics. By using the diffraction spectrum Rietveld examination, peaks of ζ-Ti_5Si_3 silicide's crystal structure were identified together with those of different TiAl correlated phases. The ζ-Ti_5Si_3 lattice parameters were discovered to be c = 5.208 Å and a = 7.545 Å. These values match the literature quite well [3]. Si alloying results in a greater quantity of γ phase at detriment of α_2 phase, but heat treatment only marginally reduces the amount of β_0 phase. The rise in γ phase that has been seen is consistent with data found in the literature.

4.4. Mechanical properties

TiAl-based alloys mechanical properties are essentially reliant on microstructures obtained during processing and/or post-processing. Mechanical properties are fundamental indications of how material components would perform in service. In this study, we have adopted the instrumented indentation testing technique also called nano-indentation testing or depth-sensing indentation. After analyzing the load-displacement curves, the mechanical properties were determined and related to the properties of commercially available GE alloy. The reported mechanical properties in this work are Young's Modulus (E), YS and UTS.

4.4.1. Microhardness

Generally speaking, microhardness gives an indication of mechanical characteristics at RT. Fig. 17 shows the microhardness of the as-built Ti-Al-Si-x(Mo+V) alloy samples produced through the modified LENS system with the addition of 0.05 g/min Mo + 0.50 g/min V and 0.05 g/min Mo + 0.35 g/min V. It is observed that additions of Mo+V does not reveal much changes in the microhardness of the as-built samples. This is evident in average microhardness values of 514$Hv_{0.5}$ and 526$Hv_{0.5}$ for alloys produce with 0.05 g/min Mo + 0.35 g/min V and 0.05 g/min Mo + 0.50 g/min V. This gives a corresponding YS of 1681 MPa and 1720 MPa, respectively. This indicates that additions Mo+V could produce a TiAl-based alloy with better mechanical properties than separate additions of Mo and V. Nevertheless, it is understood that Si causes an increase in hardness by producing ζ-Ti_5Si_3 [77]. Thus, the need to balance of the amount phases formed in the microstructure and composition to obtain better TiAl-based alloys characteristics.

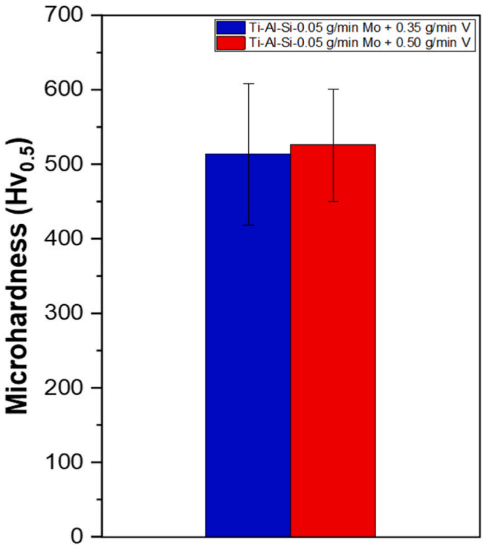

Fig. 17. Microhardness of As-Build Ti-Al-Si-x(Mo+V) Sample Processed via the Modified LENS Machine.

Fig. 18 presents the microhardness of heat-treated Ti-Al-Si-x(Mo+V) alloy samples fabricated through the modified LENS system with the addition of 0.05 g/min Mo + 0.35 g/min V and 0.05 g/min Mo + 0.50 g/min V. The values of microhardness generally reduce for heat-treated sample regardless of the mass flow rate of Mo+V added. This was attributed to very low β_0 and ζ formation including high Al composition that encourages more γ phases formation. Since γ phase has the lowest hardness value among the phases contained in the microstructure. Commonly, the heat-treated Ti-Al-Si-x(Mo+V) alloys sample

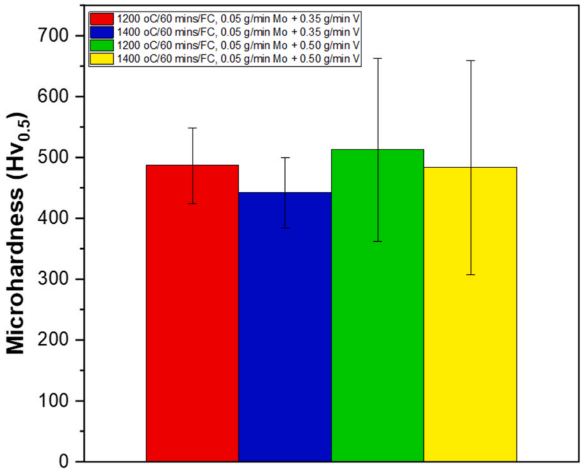

Fig. 18. Microhardness of Heat-Treated Ti-Al-0.025 g/min Si-x(Mo+V) Samples Fabricated via the Modified LENS Machine.

microhardness values shows very little disparity hardness values regardless of heat treatment temperatures. The mean microhardness values of 0.05 g/min Mo + 0.35 g/min V are 487Hv$_{0.5}$ and 442Hv$_{0.5}$ while the 0.05 g/min Mo + 0.50 g/min V gave 513Hv$_{0.5}$ and 484Hv$_{0.5}$ for heat treatment performed at 1200 °C/60 mins/FC and 1400 °C/60 mins/FC, respectively. This corresponds to 1592 MPa and 1445 MPa for 0.05 g/min Mo + 0.35 g/min V and 1678 MPa and 1583 MPa for 0.05 g/min Mo + 0.50 g/min V. This shows that Mo+V additions reduce the microhardness values of TiAl-based alloys along with the heat treatment process. Also, it was identified that improved mechanical properties are achievable through minor additions of V, Mo and Si.

From results obtained for the microhardness, it is apparent that heat treatment temperatures of 1200 °C and 1400 °C results in the decrease of microhardness for the as-built TiAl-based alloys which was recorded to be 514Hv$_{0.5}$ and 526Hv$_{0.5}$ while the annealed sample ones were between 442Hv$_{0.5}$ - 513Hv$_{0.5}$. This may be explained by the fact that unmelted aluminium dissolves at annealing temperatures and hard phases like α_2 and β_0 into the alloy matrix which in turn leads to a decline in microhardness [7]. In terms of hardness, it is known that α_2, ζ-Ti_5Si_3 and β_0 are harder than γ, α and β [80], Consequently, it can be deduced that the specimen in question does, in fact, include somewhat disordered β. Consequently, the overall microhardness profile of heat-treated samples was lesser than the as-built ones. Although, there exists hardness variation within the samples that are attributed to discrepancy of the hardness properties of constituent phases contained in the lamellar grain and microstructures examined. Moreover, as earlier stated the mean values of the sample's microhardness were reported in this study.

4.4.2. Mechanical properties from nano-indentation testing

In this study, the instrumented indentation testing technique also called nanoindentation testing or depth-sensing indentation was adopted. After analyzing the load-displacement curves, the mechanical properties were determined. The reported mechanical properties in this work are E, YS and UTS. Fig. 19 shows the load-displacement curves of the Ti-Al-Si-0.05 g/min Mo + 0.35 g/min V alloy; while Figs. 20, 21 and 22 indicates the true stress-true strain curves of the as-built and heat-treated (1200 °C and 1400 °C, respectively) Ti-Al-Si-0.05 g/min Mo + 0.35 g/min V alloy. According to a review paper by Oyen and Cook [92], all the samples in this present study exhibit elastic-plastic behaviour. But the as-built sample would be expected to demonstrate more plastic deformation than the heat-treated samples. The unloading section which describes the stiffness of the alloys suggests that the material stiffness was relatively the same. The as-built sample has a stiffness of 1.03809 $\times 10^6$ N/m, the 1200 °C/60 mins/FC sample recorded a stiffness value of 0.93312 $\times 10^6$ N/m while the 1400 °C/60 mins/FC sample stiffness is 0.94432 $\times 10^6$ N/m.

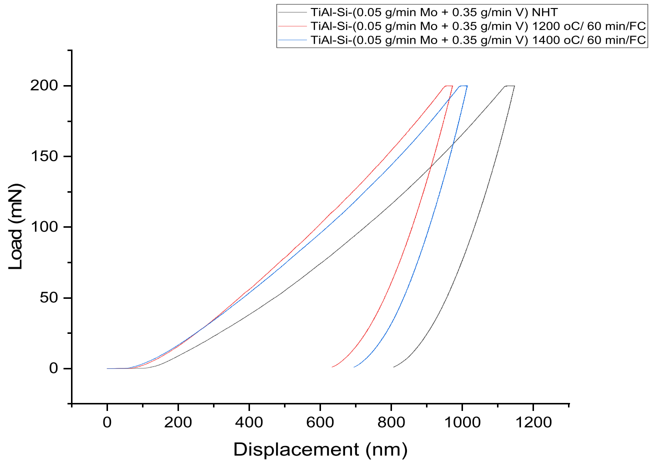

Fig. 19. Nanoindentation Load-Displacement Curves of Ti-Al-Si-0.05 g/min Mo + 0.35 g/min V Alloy.

The true stress-true strain curves are presented separately in Figs. 20, 21 and 22 for the as-built, 1200 °C/60 mins/FC and 1400 °C/60 mins/FC Ti-Al-Si-0.05 g/min Mo + 0.35 g/min V alloy, respectively. The as-built sample has a stiffness of 1.03809 $\times 10^6$ N/m, the 1200 °C/60 mins/FC sample recorded a stiffness value of 0.93312 $\times 10^6$ N/m while the 1400 °C/60 mins/FC sample stiffness is 0.94432 $\times 10^6$ N/m. As observed from Figs. 21 and 22, both heat-treated samples had higher YS and UTS compared to the as-built sample. But the 1400 °C/60 mins/FC sample showed even higher UTS compared to the 1200 °C/60 mins/FC sample. This was attributed to the FL microstructure formed by the 1400 °C/60 mins/FC alloy. The UTS and YS value of as-built alloy is 450 MPa and 325 MPa, respectively, while the E is 155 GPa. From Lerch et al. [93] and Baudana et al. [50], the E value of the as-built sample was about 7.7 % lesser than the E value of GE commercial alloy with 168 ±2 GPa at RT. But the YS in comparison to GE which is 326 MPa [93] was practically the same (0.3 % < GE). However, the GE UTS of 422 MPa [93] indicates that the as-built sample was about 6.6 % greater, thus, withstanding higher stress at RT. Consequently, these alloys would be able to perform better in terms of deformation under stress than the GE alloy. Moreover, it is expected to possess better high-temperature performance and resistance to creep owing to the strengthening mechanism of the ζ-Ti_5Si_3 phase. Si has been reported to influence to increase in strength as ζ-Ti_5Si_3 via precipitation hardening or solution strengthening [76].

Moreover, the UTS and YS value of the 1200 °C/60 mins/FC heat-treated sample is 586 MPa and 438 MPa, respectively, while the E is 191 GPa. The E value of the 1200 °C/60 mins/FC sample was about 13.7 % greater than the E value of GE alloy. Also, the YS in comparison to GE which is 326 MPa was about 34 % greater, indicating the 1200 °C/60 mins/FC sample would withstand higher stress than GE before experiencing plastic deformation. Also, the UTS indicates that the 1200 °C/60 mins/FC sample was about 38.9 % greater than GE. Therefore, the 1200 °C/60 mins/FC sample would be able to undergo more plastic deformation and would withstand higher stress at RT before fracture. The UTS and YS value of the 1400 °C/60 mins/FC heat-treated sample is 630 MPa and 368 MPa, respectively, while the E is 179 GPa.

Moreover, the E value of the 1400 °C/60 mins/FC sample was about 6.5 % greater than the E value of GE alloy at RT. Likewise, the YS in comparison to GE was about 13 % greater, indicating the 1400 °C/60 mins/FC sample would withstand higher stress than GE before experiencing plastic deformation. Also, the indicates that the 1400 °C/60 mins/FC sample was about 49.3 % greater than GE. Therefore, the 1400 °C/60 mins/FC sample would be able to undergo more plastic deformation than any of the other samples and would withstand the highest stress at RT before fracture. Although the 1400 °C/60 mins/FC sample would experience plastic deformation at lower stress compared to the 1200 °C/60 mins/FC sample, the UTS value of 630 MPa indicates that it has better toughness than the as-built, 1200 °C/60 mins/FC sample and commercially available GE alloy. Since the microstructure of the 1400 °C/60 mins/FC alloy sample displays FL microstructure, the indication of higher fracture toughness is in tandem with what is obtainable in the literature. Also, the DP microstructure of the 1200 °C/60 mins/FC explains high YS due to the presence of α_2-phase that is problematic to deform and lesser γ-phase with higher ductile performance.

Generally, lamellar microstructures exhibit better reasonable mechanical properties but the mean colonies of α_2/γ spacing lamellar has a huge effect on the performance [63]. Moreover, finer lamellae microstructures would give better strength, higher fracture toughness and creep resistance. In designing microstructures, the heat treatment strategy could be modified to achieve a balance $\gamma:\alpha_2:\beta_0$/B2 phase [94]. Hence, elimination and/or suppression of detrimental brittle phases. Due to TiAl-based alloys, brittle cracking originates from grain

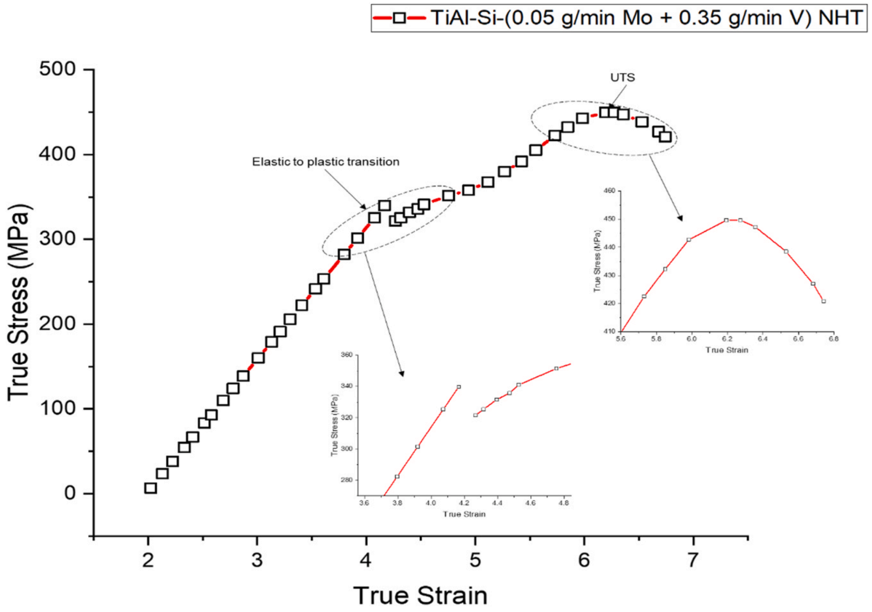

Fig. 20. True Stress-True Strain Curve of As-Built Ti-Al-Si-0.05 g/min Mo + 0.35 g/min V Alloy Showing the Regions within the Curve.

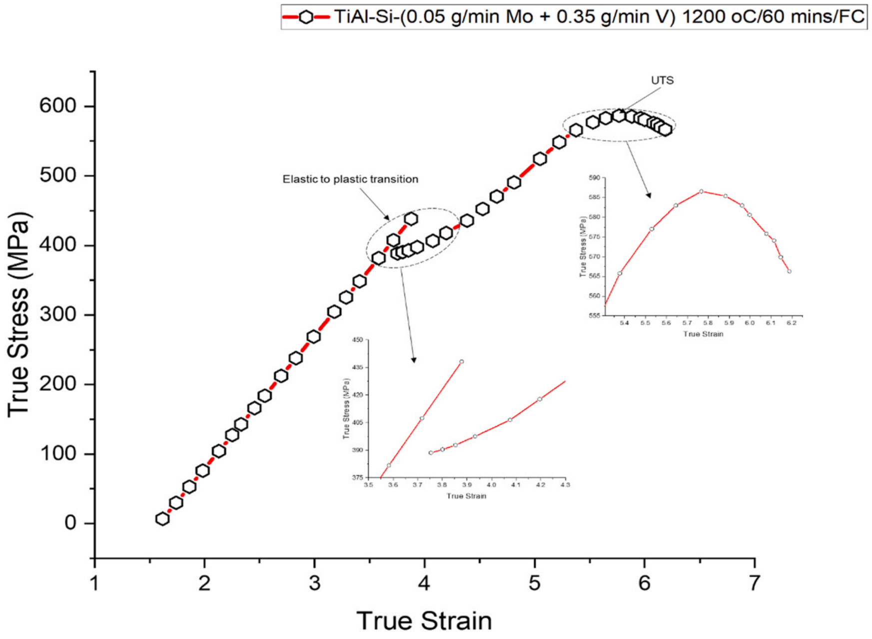

Fig. 21. True Stress-True Strain Curve of Ti-Al-Si-0.05 g/min Mo + 0.35 g/min V Heat-Treated at 1200 °C/60 mins/FC Alloy Showing the Regions within the Curve.

boundaries of lamellar colonies, thus, causing large-grained microstructures to be susceptible to cracking. The nonexistence of twinning can be connected to a lack of ductile properties [45]. The samples showing well-defined twinning in the γ-phase experienced more plastic deformation with higher ductility than the ones with lower twinning. Si has been reported to influence to increase in strength as ζ-Ti_5Si_3 via precipitation hardening or solution strengthening [76].

In TiAl-based alloys, lamellar spacing and grain size are generally highly correlated with YS. The present results can be explained via Hall-Petch type equation. As was previously mentioned, after annealing with FC instead of the as-built alloys, the grain became coarser. But as Fig. 10 illustrates, annealing at 1400 °C produced more lamellar colonies, which because of the grain coarsening enhanced the YS. Higher plasticity is generally linked to duplex microstructures with lamellae colonies as opposed to those with near γ microstructures. Consequently, the as-built alloys' residual stress was efficiently removed by annealing them at 1200°C, which raised UTS [57]. However, it was determined that the improved mechanical properties were due to collective influence of the reinforcing β_0 and ζ-Ti_5Si_3 phases. However, the amount of the brittle phases β_0, α_2, and ζ-Ti_5Si_3 is slightly reduced due to the decrease in β_0 phase and formation of lamellae structure after HT at 1400°C with FC. This successfully boosted the plasticity and resulted in a large rise in YS.

It is well acknowledged that ordered intermetallic TiAl-based alloy deforms via a dislocation glide, which can be quite challenging to operate [21]. Enhancing the tendency for twinning in γ-phase also improves plasticity. The alloying additions may diminish the γ-phase stacking fault energy; thus, this enhancement can be realized. Furthermore, it has been shown that the lamellar spacing, λ, has a significant impact; for any λ between 4100 nm and the YS, the connection is of the

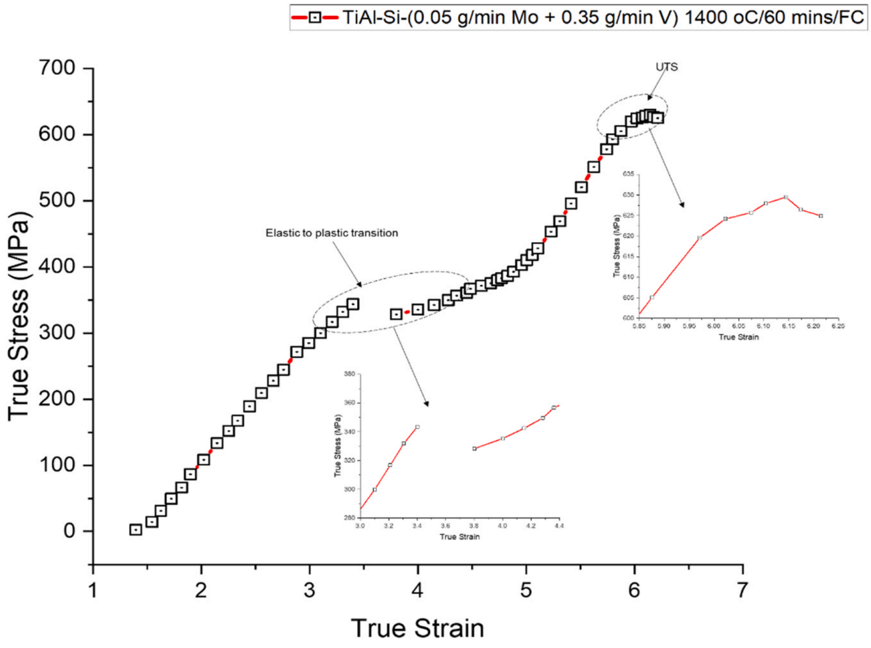

Fig. 22. True Stress-True Strain Curve of Ti-Al-Si-0.05 g/min Mo + 0.35 g/min V Heat-Treated at 1400 °C/60 mins/FC Alloy Showing the Regions within the Curve.

standard Hall–Petch type [80]. Therefore, ductility and work hardening coefficient drop as λ decreases, whereas the YS increases. Depending on whether disordered β or ordered B2 (β_0) is preserved after HT, the existence of the B2/β phases could have a positive or negative effect on RT ductility. Once more, even minor alterations to the resulting microstructures have the potential to significantly worsen embrittlement and may not be regarded as a good option for improving mechanical properties overall. In summary, the best overall mechanical properties are found in the Ti-Al-Si-0.05 g/min Mo + 0.35 g/min V alloy that has been heat-treated at 1200 °C for 60 minutes under FC conditions. In high-Al TiAl alloys, the studied alloy exhibits competitive characteristics. The emergence of stronger phases inside the matrix structure and the grain interfaces following heat treatment were identified as the primary causes of the enhanced UTS and YS.

4.5. *Tribological behaviour*

To ascertain the durability of TiAl-based alloy components in service, evaluating the tribological behaviour and high-temperature stability is very crucial. This represents a critical issue for aero-engine applications as the turbocharger operating temperature range is between 700 and 950 °C. Stability over time in a surrounding environment of air, where the mechanical characteristics and microstructure must be maintained throughout the part's lifespan, is a crucial feature of elevated temperatures TiAl-based alloys. Fig. 23 presents the CoF and wear rate of the in-situ developed Ti-Al-Si-0.05 g/min Mo + 0.35 g/min V alloy prior and post heat treatments. As observed from Fig. 23, the CoF generally reduces from the as-built sample (0.586) to the 1200 °C/60 mins/FC sample (0.498) and the 1400 °C/60 mins/FC sample (0.492) having the lowest value of CoF. However, the wear rate does not for the same pattern. The sample heat-treated at 1200 °C/60 mins/FC showed the maximum wear rate value of 1.645 $\times 10^{-4}$ mm^3/N/m, followed by the as-built sample with a value of 4.266 $\times 10^{-5}$ mm^3/N/m while the sample heat-treated at 1400 °C/60 mins/FC had the least wear rate of 2.88 $\times 10^{-6}$ mm^3/N/m.

The tribological behaviour of the quintenary Ti-Al-Si-Mo-V alloy is

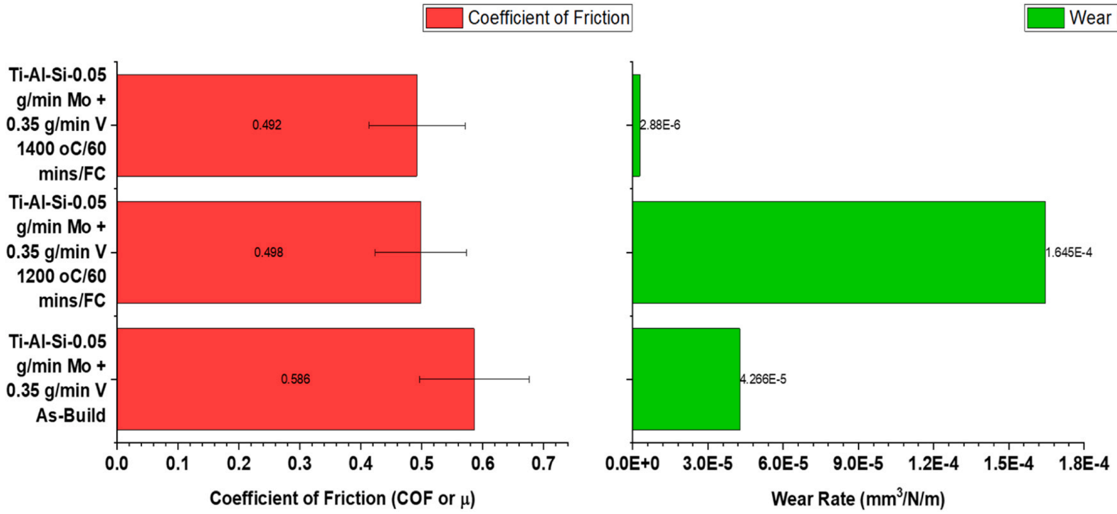

Fig. 23. Showing Coefficient of Friction and Wear Rate of Ti-Al-Si-0.05 g/min Mo + 0.35 g/min V Alloy.

highly unusual because the high wear rate recorded by the 1200 °C/60 mins/FC sample was not expected. However, the high rate to wear is indicative of more material removal during the sliding test. Moreover, the as-built sample had a higher wear rate than the 1400 °C/60 mins/FC. This was expected due to the FL microstructure in the 1400 °C/60 mins/FC sample while the as-built sample exhibited more precipitates of hard phases like α_2, β_0 and ζ-Ti_5Si_3. Evidently, there is no huge change in CoF but it increases from the as-built, 1200 °C/60 mins/FC with the 1400 °C/60 mins/FC samples having the highest CoF. This may be credited to hard phases formed by the DED process of the TiAl-based alloy having a better load bearing capacity than the samples that have been heat-treated [7]. Additionally, fast cooling in alloy development—that results in strong resistance to deformation and small grain size —is linked to the DED process manufacturing. The Hall-Petch equation could be connected to generate matrices with strong resistance to deformation and reduced grain sizes. Additionally, phases created by laser deposition prevented the alloy from wearing off too quickly and may have improved the TiAl-based alloy's surface [7]. This explains why the as-built sample's wear rate is noticeably lower than that of the heat-treated samples.

4.6. *Thermogravimetric behaviour*

The behaviour of TiAl alloys in the presence of oxygen at elevated temperatures is an essential feature of high-temperature applications for advanced supersonic aircraft's engines and gas turbines [95]. This represents a critical issue for aero-engine applications as the turbocharger operating temperature range is between 700 and 950 °C. The long-term stability is an important characteristic because the microstructure and mechanical properties needs to be sustained during the section's lifespan [96]. Fig. 24 shows the TGA curves of the Ti-Al-Si-0.05 g/min Mo + 0.35 g/min V alloy. The results of the TGA presents the change in mass against temperature relative to the initial mass of the sample per unit area. Positive mass change means that the oxides products formed are solid and remained attached to the surface of the samples. This mass gain depends on the chemical bonding formed with air (oxygen and nitrogen). In situations where spalling of the solid scale occurs or oxides products are volatile, negative mass change is recorded which indicted that alloy components are lost [97]. It was observed that mass loss for the as-built sample was in the negative direction with a slight reduction in mass at 130 °C. The cumulative mass loss continued to reduce up to 800 °C which results in a slight rise in mass in the positive direction. However, the mass gained at that temperature could not balance the initial material loss. The heat-treated sample demonstrated better high-temperature stability but most of the mass loss was also in the negative direction indicating that the formation of corrosion products leads to alloy components loss or the layers formed on the surface of the samples are volatile.

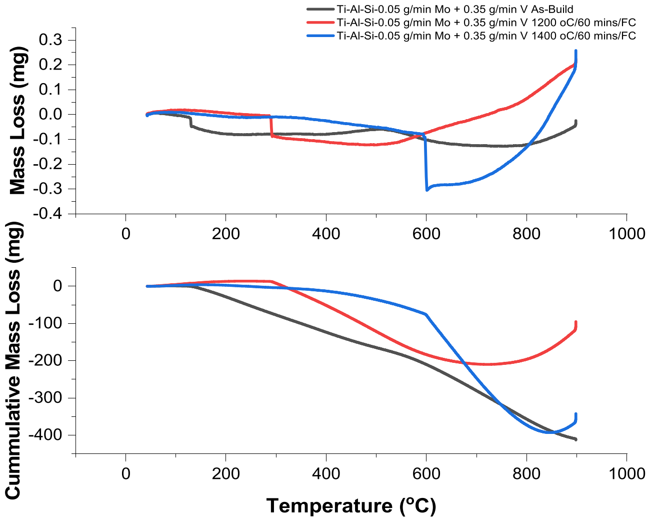

Fig. 24. : TGA Curves of Ti-Al-Si-0.05 g/min Mo + 0.35 g/min V Alloy.

A slight drop in mass was noticed for the 1200 °C/60 mins/FC sample at 292 °C while the 1400 °C/60 mins/FC sample also experienced a drastic decrease in mass at 600 °C. Generally, all the samples displayed positive mass changes at temperatures above 800 °C, denoting that the oxide scales are being attached to the samples. Thus, the alloys which demonstrate less spalling would be more suitable for turbocharger wheel applications because the operating temperature is between 850 °C to 900 °C. It can be problematic to predict oxidation behaviour of TiAl-based alloys having varying microstructures and compositions. Also, oxidation responses are determined by the experimental set-up, temperature, type of atmosphere used and oxygen impurity initially within the alloy [98]. The presence of Si has been reported to minimize the mechanisms of oxidation due to the barrier effects induced via silica and silicide. But layer exfoliation by Si addition leads to a deteriorating effect on oxidation [98]. Mo enriches the TiAl alloy layer to form a metals/oxide interface, thereby decreasing the oxygen diffusion and Ti into the bulk material. The benefits of Mo are ascribed to its capability to increase alumina at the outer section of oxide layer and reduce simultaneously the oxygen solubility into the whole material. Resistance to oxidation presents a convincing restriction for wide-ranging use of TiAl alloys in automotive and aerospace fields. The resistance to oxidation is mainly dependent on the Al composition because it influences the ratio of titanium oxides and alumina inside the oxide scales based on the concentration from the built material. The alumina layer demonstrates passivation behaviour and grows slowly compared to titanium oxides formation. The Al content also determines the ratio of α_2 and γ phases within the microstructures which consequently influences resistance to oxidation because Al distribution in γ-TiAl is faster than α_2-Ti_3Al.

Even at temperatures above 600 °C, the present alloy heat-treated sample at 1200 °C/60 mins/FC relatively maintains mass gain values compared with other samples. The findings demonstrated that temperature had a major impact on oxidation and that mass acquired increased dramatically as exposure temperature rose. In the first phase, the mass-change curves were nearly parallel (0–100 °C), indicating that the mass changes sharply, as oxide scale begin to form on the surface of the samples [31]. Hence, it can be noted that the DP microstructure with FL grains is more advantageous to achieve the improved resistance to oxidation for γ-TiAl alloys; while specimen with FL microstructure was slightly resistance to oxidation. Conversely, for as-built sample, it demonstrated the weakest resistance to oxidation based of the TGA results. Increased mass gain values result from the TiO_2 phase, which is much probable to be developed in α_2 phase, as previously explained. The reason for this is that finer grain sizes lead to an intensity of grain colonies which in turn increases the amount of potential sites of nucleation for the creation of scales with finer oxides [19]. Furthermore, the sort of alloy microstructure has a significant effect on the oxidation kinetics of TiAl-based alloys. In contrast to equiaxed grains that developed following heat treatment, the alloy having lamellar microstructure produced a protective alumina passivation film, indicating a greater potential to produce a non-protective oxide film. According to preliminary research on references [19], the γ and α_2 phase compositions are conducive to the development of Al_2O_3 and TiO_2 oxide scales, respectively. As a result, the stable oxide scale on the TiO_2 scale can be obtained in the fine colonies grains of α_2/γ-lamellar, leading to the formation of a stable oxide film throughout the alloy exterior. In comparison to conventional γ-TiAl alloys, the DED-fabricated alloy's homogeneous microstructure with duplex microstructure and lamellae colonies is advantageous for achieving high oxidation resistance.

5. Prospects, significance and limitations

The DED technology was successfully adopted to fabricate TiAl-based alloys with addition of Si, Mo and V via In-situ alloying via a modified LENS system. Considering that most research on TiAl alloys is aimed at the improvement of mechanical properties. Also, the GE-4822 alloy which is presently the most widely accepted and benchmarked TiAl-based alloy for aerospace industry that has been effectively fabricated into marketable turbine blades by GE using the EBM process. A summary of the mechanical properties of this current TiAl-based in comparison to the GE alloy is presented in Fig. 25. Therefore, it could be deduced that the alloys produced in this work could compete favourably with GE-4822 alloy for industrial applications. Since this work is intended for aerospace applications, thus, it is worthy to note that comparing of properties gotten in these alloys with commercially available GE alloy properties pertinent. Base on the success recorded in this work, this manufacturing approach could be further improved for effective production of TiAl-based alloys for engineering components.

It has been reported by Nochovnaya et al. [99], that the most recent TiAl alloy developed and patented as a commercial alloy is the TNB/TNM alloy invented in 2007. This means that in the last seventeen years, there has not been any newly developed alloy that could compete favourably with the alloys currently available in the market. The results achieved indicated that the mechanical properties of the developed alloys were improved, although a trade-off needs to be critically considered for cost and density when fabricating actual parts using these alloys. It ought to be well-thought-out that to attain the anticipated material properties, the processing-texture-microstructure relationship needs to be considered. In the synergy of the alloy, specific parts design and development need to take into consideration the requirement of several structures for increasing the commercial use of high-temperature applications for TiAl-based alloys.

Moreover, this alloy was developed with a focus for potential applications that would be suitable for the aerospace engine parts like the turbo charger wheels and LPT blades. The effective development of alloys presented in this research is quite significant because it would aid in the reducing the early malfunction in service of parts produced with TiAl alloys owing to innovative properties acquired through the advanced LENS technology. in This has also broadened the understanding of using the LENS technique for the manufacture of TiAl alloy via in-situ alloying. This will further lead to advance studies on the development of engineering materials that will subsequently improve knowledge and innovation in AM.

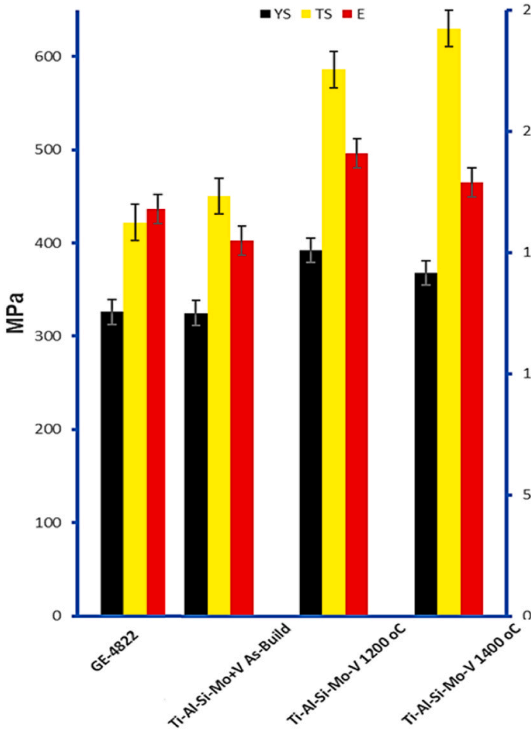

Fig. 25. Summary of the Mechanical Properties of Fabricated Alloys Produced Via LENS Machine in Comparison to GE-4822 Commercial Alloy.

Comparing the mechanical properties of the LENS produced alloys with that of traditionally manufactured equivalents is one of the requirements for using them in engineering applications. As stated in Section 4.4, good mechanical properties were obtained for the Ti-Al-Si-Mo-V alloy fabricated by the in-situ alloying LENS technique. The alloys were fabricated and heat-treated to achieve duplex microstructures demonstrating better RT mechanical properties. Overall, compared to the previously developed TiAl alloys that were produced conventionally and using AM, the performance of the produced alloys based on this study is superior. The alloy's microstructure can be readily modified through heat treatments to produce an array of microstructures dependent on the requirements of the application. However, these alloys like other TiAl-based alloys are still prone to cracking during fabrication due to their inherent brittleness.

Since this work is intended for aerospace applications, but the main characteristic needed for turbine wheel material is durability against centrifugal stress produced when revolving. Nevertheless, this alloy could be adopted to fabricate LPT, HPC and turbocharger wheels in the aerospace industry. It is worthy to note that comparing the properties gotten in these alloys with commercially available GE-4822 alloy properties was mainly reliant on the microstructure and the fabrication process used.

6. Conclusions

In this present research, TiAl-based alloys were successfully fabricated via in-situ alloying by means of DED processing with Si, Mo and V as alloying elements followed by heat treatment at 1200 °C and 1400 °C for 60 mins then FC. An investigation was conducted to understand the impacts of the alloying materials on the heat-treated DED LENS fabricated alloy's microstructure, microhardness, nanomechanical characteristics, and wear. The experiment's findings and the accompanying studies lead to a number of conclusions, which are summed up as follows:

- ✓ The as-built Ti-Al-Si-Mo-V alloys demonstrates $\alpha_2+\gamma$ columnar grains with β-phase and ζ-Ti_5Si_3-phase noticed both at grain interfaces and within the lamellar grains. While the heat-treated DP and FL microstructures for 1200 °C and 1400 °C, respectively.
- ✓ The phase analysis of the LENS fabricated alloys identified the same type of phases but the composition of the phases formed varied. Small amount of the β_0 formed in the as-built alloys was attributed to the Mo content of approximately 1.0 at% showing low intensity peaks in the XRD results except for the heat-treated samples. Thus, implying that transformation of phases transpired during heat treatment.
- ✓ The LENS fabricated alloy's UTS were about 6.6–49.3 % greater than GE-4822 alloy; while the YS were up to 34 % greater than GE alloy based on the nanomechanical data. The samples demonstrated higher plastic deformation levels compared to GE for both the as-built and heat-treated samples, thus, indicating that it possesses better fracture toughness than commercially available GE alloy. Consequently, these alloys would be able to perform very well as material for aero-engines parts.
- ✓ The degree of enhancement in materials properties for alloys depends on the heat treatment carried out and the amount of precipitate phases produced. Therefore, based on these results it was implied that the Ti-Al-Si-Mo-V alloys would be more suitable

turbocharger wheel applications because the operating temperature is between 850 °C to 900 °C.

- ✓ The simulation result implies that cracking is avoided by increasing the processing temperature and continuous heating during processing. It was deduced that the processing temperature does not affect the maximum stress experienced by the TiAl alloy but the minimum stress level changes with processing temperatures.

Ethical Approval

Not Applicable

CRediT authorship contribution statement

S.A. Raji: Conceptualization, Data curation, Formal analysis, Investigation, Methodology, Software, Validation, Visualization, Roles/Writing - original draft, Writing - review & editing **A.P.I. Popoola:** Funding acquisition, Methodology, Project administration, Resources, Supervision, Validation **O.M. Popoola:** Funding acquisition, Investigation, Project administration, Project administration, Software, Supervision, Writing - review & editing **S.L. Pityana:** Conceptualization, Formal analysis, Funding acquisition, Methodology, Project administration, Resources, Software, Supervision, Validation, Visualization, Writing - review & editing **M. Tlotleng:** Conceptualization, Data curation, Formal analysis, Investigation, Methodology, Resources, Supervision, Validation, Roles/Writing - original draft;

Declaration of Competing Interest

The authors declare the following financial interests/personal relationships which may be considered as potential competing interests. Raji SA has patent Alloy Produced By Additive Manufacturing pending to SA Raji, API Popoola, SL Pityana, M Tlotleng and OM Popoola. If there are other authors, they declare that they have no known competing financial interests or personal relationships that could have appeared to influence the work reported in this paper.

Acknowledgment

The following organisations are acknowledged by the authors: National Research Fund (NRF), South Africa with Surface Engineering Research Laboratory (SERL) under the Leadership of Prof. API Popoola (The Advanced Engineering Research Group); African Laser Centre-National Laser Centre, CSIR (ALC-NLC, CSIR), Project Number LHIP500 Task ALCS100; and Council of Scientific and Industrial Research (CSIR) South Africa. Additionally, acknowledged by the authors is the Department of Chemical, Metallurgical, and Materials Engineering at Tshwane University of Technology's Faculty of Engineering and the Built Environment in Pretoria, South Africa. Additionally, we thank Mr. Paul Lekoadi and Mr. Nana Kwamina Kum Arthur of the CSIR's Laser Materials Processing Group for their assistance in carrying out the experiment.

Appendix A. Supporting information

Supplementary data associated with this article can be found in the online version at doi:10.1016/j.nxmate.2024.100329.

References

[1] P. Erdely, R. Werner, E. Schwaighofer, H. Clemens, S. Mayer, In-situ study of the time–temperature-transformation behaviour of a multi-phase intermetallic β-stabilised TiAl alloy, Intermetallics 57 (2015) 17–24, https://doi.org/10.1016/j.intermet.2014.09.011.

[2] S. Motha, N. Maledi, M. Tlotleng, Characterization of Mn micro alloyed TiAl fabricated using laser engineered net shaping (LENS), Mater. Today.: Proc. 62 (2022) S163–S175, https://doi.org/10.1016/j.matpr.2022.04.817.

[3] M. Musi, B. Galy, A. Stark, N. Schell, M. Hantcherli, J.P. Monchoux, A. Couret, H. Clemens, P. Spoerk-Erdely, How Si affects the microstructural evolution and phase transformations of intermetallic γ-TiAl based alloys, Materialia 24 (2022) 101475, https://doi.org/10.1016/j.mtla.2022.101475.

[4] M. Teschke, J. Moritz, J. Tenkamp, A. Marquardt, C. Leyens, F. Walther, Defect-based characterization of the fatigue behavior of additively manufactured titanium aluminides, Int. J. Fatigue 163 (2022) 107047, https://doi.org/10.1016/j.ijfatigue.2022.107047.

[5] G. Baudana, S. Biamino, B. Klöden, A. Kirchner, T. Weißgärber, B. Kieback, M. Pavese, D. Ugues, P. Fino, C. Badini, Electron beam melting of Ti-48Al-2Nb-0.7 Cr-0.3 Si: feasibility investigation, Intermetallics 73 (2016) 43–49, https://doi.org/10.1016/j.intermet.2016.03.001.

[6] H.A. Soliman, M. Yakout, M. Elbestawi, Laser powder bed fusion of titanium aluminides using sequential thermal scanning strategy, J. Manuf. Process. 83 (2022) 438–457, https://doi.org/10.1016/j.jmapro.2022.09.014.

[7] L.R. Kanyane, A.P.I. Popoola, S.L. Pityana, M. Tlotleng, Heat-treatment effect on anti-corrosion behaviour and tribological properties of LENS in-situ synthesized titanium aluminide, Int. J. Lightweight Mater. Manuf. 5 (2022) 153–161, https://doi.org/10.1016/j.ijlmm.2021.11.006.

[8] W. Liu, J. DuPont, 2002. Fabrication of titanium aluminide matrix composites by laser engineered net shaping. In 2002 International Solid Freeform Fabrication Symposium. https://doi.org/10.26153/tsw/3423.

[9] Q. Wang, R. Chen, Y. Yang, S. Wu, J. Guo, H. Ding, Y. Su, H. Fu, Effects of lamellar spacing on microstructural stability and creep properties in β-solidifying γ-TiAl alloy by directional solidification, Mater. Sci. Eng.: A 711 (2018) 508–514, https://doi.org/10.1016/j.msea.2017.11.080.

[10] S. Catchpole-Smith, A.T. Clare, In-situ synthesis of titanium aluminides by direct metal deposition, J. Mater. Process. Technol. 239 (2017) 230–239, https://doi.org/10.1016/j.jmatprotec.2016.08.031.

[11] P.L. Narayana, C.L. Li, S.W. Kim, S.E. Kim, A. Marquardt, C. Leyens, N.S. Reddy, J. T. Yeom, J.K. Hong, High strength and ductility of electron beam melted β stabilized γ-TiAl alloy at 800C, Mater. Sci. Eng.: A 756 (2019) 41–45, https://doi.org/10.1016/j.msea.2019.03.114.

[12] X. Xu, H. Ding, H. Huang, H. Liang, R. Chen, J. Guo, H. Fu, Effect of V on the microstructure and brittle-to-ductile transition of directionally solidified high-Nb TiAl alloy, Intermetallics 142 (2022) 107455, https://doi.org/10.1016/j.intermet.2021.107455.

[13] W. Yu, J. Zhou, Y. Yin, Z. Tu, X. Feng, H. Nan, J. Lin, X. Ding, Effects of heat treatments on microstructures of TiAl alloys, Int. J. Miner., Metall. Mater. 29 (2022) 1225–1230, https://doi.org/10.1007/s12613-021-2252-z.

[14] R. Biswas, A.S. Kuar, S. Mitra, Multi-objective optimization of hole characteristics during pulsed Nd: YAG laser microdrilling of gamma-titanium aluminide alloy sheet, Opt. Lasers Eng. 60 (2014) 1–11, https://doi.org/10.1016/j.optlaseng.2014.03.014.

[15] Q. Wang, H. Ding, H. Zhang, R. Chen, J. Guo, H. Fu, Variations of microstructure and tensile property of γ-TiAl alloys with 0–0.5 at% C additives, Mater. Sci. Eng.: A 700 (2017) 198–208, https://doi.org/10.1016/j.msea.2017.06.019.

[16] J. Bieske, M. Franke, M. Schloffer, C. Körner, Microstructure and properties of TiAl processed via an electron beam powder bed fusion capsule technology, Intermetallics 126 (2020) 106929, https://doi.org/10.1016/j.intermet.2020.106929.

[17] M. Kastenhuber, B. Rashkova, H. Clemens, S. Mayer, Effect of microstructural instability on the creep resistance of an advanced intermetallic γ-TiAl based alloy, Intermetallics 80 (2017) 1–9, https://doi.org/10.1016/j.intermet.2016.09.007.

[18] D. Srivastava, I.T.H. Chang, M.H. Loretto, The optimisation of processing parameters and characterisation of microstructure of direct laser fabricated TiAl alloy components, Mater. Des. 21 (2000) 425–433, https://doi.org/10.1016/S0261-3069(99)00091-6.

[19] P.L. Narayana, J.H. Kim, D.W. Yun, S.E. Kim, N.S. Reddy, J.T. Yeom, D. Seo, J. K. Hong, High temperature isothermal oxidation behavior of electron beam melted multi-phase γ-TiAl alloy, Intermetallics 141 (2022) 107424, https://doi.org/10.1016/j.intermet.2021.107424.

[20] B.K. Singh, V.A. Kumar, R.K. Gupta, A.K. Kanjarla, Evolution of microstructure in niobium rich (α2+ γ) based titanium aluminide alloy during hot compression, Mater. Sci. Eng.: A 754 (2019) 708–718, https://doi.org/10.1016/j.msea.2019.03.111.

[21] S.Z. Zhang, Y.B. Zhao, C.J. Zhang, J.C. Han, M.J. Sun, M. Xu, The microstructure, mechanical properties, and oxidation behavior of beta-gamma TiAl alloy with excellent hot workability, Mater. Sci. Eng.: A 700 (2017) 366–373, https://doi.org/10.1016/j.msea.2017.06.025.

[22] R.R. Xu, H. Li, M.Q. Li, Flow softening mechanism in isothermal compression of β-solidifying γ-TiAl alloy, Mater. Des. 186 (2020) 108328, https://doi.org/10.1016/j.matdes.2019.108328.

[23] Y. Wu, H. Wang, X. Ma, J. Wang, F. Cheng, J. Han, X. Cheng, A. Li, B. He, Fabrication of TiAl alloy with no multiple heat-affected bands using continuous direct energy deposition, Mater. Lett. 281 (2020) 128581, https://doi.org/10.1016/j.matlet.2020.128581.

[24] B. Lin, W. Chen, Y. Yang, F. Wu, Z. Li, Anisotropy of microstructure and tensile properties of Ti–48Al–2Cr–2Nb fabricated by electron beam melting, J. Alloy. Compd. 830 (2020) 154684, https://doi.org/10.1016/j.jallcom.2020.154684.

[25] Y. Guo, Y. Liang, J. Lin, In situ synthesis of nano/micron Ti2AlC reinforced high-Nb TiAl composites: Microstructure and mechanical properties, Intermetallics 159 (2023) 107937, https://doi.org/10.1016/j.intermet.2023.107937.

[26] J. Zhang, Y. Wu, X. Cheng, S. Zhang, H. Wang, Study of microstructure evolution and preference growth direction in a fully laminated directional micro-columnar

TiAl fabricated using laser additive manufacturing technique, Mater. Lett. 243 (2019) 62–65, https://doi.org/10.1016/j.matlet.2019.01.137.

[27] J. Han, S. Xiao, J. Tian, Y. Chen, L. Xu, X. Wang, Y. Jia, H.K.S. Rahoma, Z. Du, S. Cao, Microstructure characterization, mechanical properties and toughening mechanism of TiB2-containing conventional cast TiAl-based alloy, Mater. Sci. Eng.: A 645 (2015) 8–19, https://doi.org/10.1016/j.msea.2015.07.092.

[28] J. Bresler, S. Neumeier, M. Ziener, F. Pyczak, M. Göken, The influence of niobium, tantalum and zirconium on the microstructure and creep strength of fully lamellar γ/α2 titanium aluminides, Mater. Sci. Eng.: A 744 (2019) 46–53, https://doi.org/10.1016/j.msea.2018.11.152.

[29] Z. Zhou, R. Liu, Y. Shen, Y. Liu, P. Wang, Y. Cui, R. Yang, Microstructural evolution and embrittlement of a β-solidifying γ-TiAl alloy during exposure at 700° C, Mater. Sci. Eng.: A 852 (2022) 143704, https://doi.org/10.1016/j.msea.2022.143704.

[30] J. Lapin, M. Štamborská, T. Pelachová, O. Bajana, Fracture behaviour of cast in-situ TiAl matrix composite reinforced with carbide particles, Mater. Sci. Eng.: A 721 (2018) 1–7, https://doi.org/10.1016/j.msea.2018.02.077.

[31] Y. Wang, C. Liu, T. Ma, Y. Liu, Y. Zhang, L. Zhou, Improvement in oxidation resistance of TiAl alloys by in-situ precipitation of Ti2AlC at the interface of α2 and γ lamellae, Corros. Sci. 208 (2022) 110639, https://doi.org/10.1016/j.corsci.2022.110639.

[32] Z. Liu, G. Yin, X. Zhu, Q. Zhou, Microstructure, texture and tensile properties as a function of laser power of Ti48Al2Cr2Nb5Ta alloy prepared by laser additive manufacturing, J. Manuf. Process. 73 (2022) 624–632, https://doi.org/10.1016/j.jmapro.2021.11.039.

[33] F.S. Franzén J. Karlsson, Titanium Aluminide Manufactured by Electron Beam Melting. (Master's Thesis), Chalmers University of Technology: (2010) 37. https://hdl.handle.net/20.500.12380/127716.

[34] H.A. Soliman, M. Elbestawi, Titanium aluminides processing by additive manufacturing–a review, Int. J. Adv. Manuf. Technol. 119 (2022) 5583–5614, https://doi.org/10.1007/s00170-022-08728-w.

[35] Y. Guo, S. Xiao, Y. Chen, J. Tian, Z. Zheng, L. Xu, High temperature tensile properties and fracture behavior of Y2O3-bearing Ti-48Al-2Cr-2Nb alloy, Intermetallics 126 (2020) 106933, https://doi.org/10.1016/j.intermet.2020.106933.

[36] S. Dong, Y. Qu, R. Chen, G. Li, W. Zhang, Q. Wang, H. Fang, J. Guo, B. Yu, Proper (Nb, Fe) co-alloyed TiAl-based alloy with good hot deformation processing capability, Intermetallics 153 (2023) 107780, https://doi.org/10.1016/j.intermet.2022.107780.

[37] C. Hong, D. Gu, D. Dai, M. Alkhayat, W. Urban, P. Yuan, S. Cao, A. Gasser, A. Weisheit, I. Kelbassa, M. Zhong, Laser additive manufacturing of ultrafine TiC particle reinforced Inconel 625 based composite parts: Tailored microstructures and enhanced performance, Mater. Sci. Eng.: A 635 (2015) 118–128, https://doi.org/10.1016/j.msea.2015.03.043.

[38] D. Wang, C. Wen, Y. Chang, W. Lin, S.C. Chen, Ultrafast laser-enabled 3D metal printing: a solution to fabricate arbitrary submicron metal structures, Precis. Eng. 52 (2018) 106–111, https://doi.org/10.1016/j.precisioneng.2017.11.015.

[39] D. Huang, Y. Dong, H. Chen, Y. Zhou, M.X. Zhang, M. Yan, Effects of processing parameters on a β-solidifying TiAl alloy fabricated by laser-based additive manufacturing, Microstructures 2 (2022) 2022019, https://doi.org/10.20517/microstructures.2022.17.

[40] S.A. Raji, A.P.I. Popoola, S. Pityana, O.M. Popoola, M. Tlotleng, Microstructure and micro-hardness properties of in-situ lens fabricated Ti-Al-Si-xV Alloys (EDP Sciences), MATEC Web Conf. 370 (2022) 03010, https://doi.org/10.1051/matecconf/202237003010.

[41] T. Duda, L.V. Raghavan, 3D metal printing technology, IFAC-Pap. 49 (2016) 103–110, https://doi.org/10.1016/j.ifacol.2016.11.111.

[42] F. Ning, Y. Hu, Z. Liu, W. Cong, Y. Li, X. Wang, Ultrasonic vibration-assisted laser engineered net shaping of Inconel 718 parts: a feasibility study, Procedia Manuf. 10 (2017) 771–778, https://doi.org/10.1016/j.promfg.2017.07.074.

[43] C. Kenel, G. Dasargyri, T. Bauer, A. Colella, A.B. Spierings, C. Leinenbach, K. Wegener, Selective laser melting of an oxide dispersion strengthened (ODS) γ-TiAl alloy towards production of complex structures, Mater. Des. 134 (2017) 81–90, https://doi.org/10.1016/j.matdes.2017.08.034.

[44] W. Gao, Y. Zhang, D. Ramanujan, K. Ramani, Y. Chen, C.B. Williams, C.C. Wang, Y. C. Shin, S. Zhang, P.D. Zavattieri, The status, challenges, and future of additive manufacturing in engineering, Comput. -Aided Des. 69 (2015) 65–89, https://doi.org/10.1016/j.cad.2015.04.001.

[45] S.E. Hoosain, S. Pityana, C.S. Freemantle, M. Tlotleng, Heat treatment of in situ laser-fabricated titanium aluminide, Metals 8 (2018) 655, https://doi.org/10.3390/met8090655.

[46] S.K. Rittinghaus, U. Hecht, V. Werner, A. Weisheit, Heat treatment of laser metal deposited TiAl TNM alloy, Intermetallics 95 (2018) 94–101, https://doi.org/10.1016/j.intermet.2018.02.002.

[47] M. Li, X. Wu, Y. Yang, Q. Wei, C. Yan, C. Cai, J. Liu, W. Li, Y. Shi, TiAl/RGO (reduced graphene oxide) bulk composites with refined microstructure and enhanced nanohardness fabricated by selective laser melting (SLM), Mater. Charact. 143 (2018) 197–205, https://doi.org/10.1016/j.matchar.2018.05.040.

[48] W. Li, J. Liu, Y. Zhou, S. Li, S. Wen, Q. Wei, C. Yan, Y. Shi, Effect of laser scanning speed on a Ti-45Al-2Cr-5Nb alloy processed by selective laser melting: microstructure, phase and mechanical properties, J. Alloy. Compd. 688 (2016) 626–636, https://doi.org/10.1016/j.jallcom.2016.07.206.

[49] H. Yue, Y. Chen, X. Wang, F. Kong, Effect of beam current on microstructure, phase, grain characteristic and mechanical properties of Ti-47Al-2Cr-2Nb alloy fabricated by selective electron beam melting, J. Alloy. Compd. 750 (2018) 617–625, https://doi.org/10.1016/j.jallcom.2018.03.343.

[50] G. Baudana, S. Biamino, B. Klöden, A. Kirchner, T. Weißgärber, B. Kieback, M. Pavese, D. Ugues, P. Fino, C. Badini, Electron beam melting of Ti-48Al-2Nb-0.7 Cr-0.3 Si: feasibility investigation, Intermetallics 73 (2016) 43–49, https://doi.org/10.1016/j.intermet.2016.03.001.

[51] M. Todai, T. Nakano, T. Liu, H.Y. Yasuda, K. Hagihara, K. Cho, M. Ueda, M. Takeyama, Effect of building direction on the microstructure and tensile properties of Ti-48Al-2Cr-2Nb alloy additively manufactured by electron beam melting, Addit. Manuf. 13 (2017) 61–70, https://doi.org/10.1016/j.addma.2016.11.001.

[52] P. Gao, Z. Wang, X. Zeng, Effect of process parameters on morphology, sectional characteristics and crack sensitivity of Ti-40Al-9V-0.5 Y alloy single tracks produced by selective laser melting, Int. J. Lightweight Mater. Manuf. 2 (2019) 355–361, https://doi.org/10.1016/j.ijlmm.2019.04.001.

[53] M. Doubenskaia, A. Domashenkov, I. Smurov, P. Petrovskiy, Study of selective laser melting of intermetallic TiAl powder using integral analysis, Int. J. Mach. Tools Manuf. 129 (2018) 1–14, https://doi.org/10.1016/j.ijmachtools.2018.02.003.

[54] A.R.C. Sharman, J.I. Hughes, K. Ridgway, Characterisation of titanium aluminide components manufactured by laser metal deposition, Intermetallics 93 (2018) 89–92, https://doi.org/10.1016/j.intermet.2017.11.013.

[55] M. Tlotleng, S.L. Pityana, 2017. In-situ alloyed LENS additively manufactured TiAl-Nb structure. In: 18th Annual International Rapid Product Development Association of South Africa (RAPDASA), Durban ICC, South Africa, 7-10 November 2017: 251-25. http://hdl.handle.net/10204/9855.

[56] M. Tlotleng, S. Pityana, S. Motha, Insights on niobium micro-alloyed laser in situ synthesised gamma titanium aluminide alloys, Appl. Sci. 13 (2023) 5725, https://doi.org/10.3390/app13095725.

[57] D. Huang, X. Yao, Y. Zhou, Q. Zhu, Y. Tang, H. Huang, M.X. Zhang, M. Yan, Tailoring microstructure and mechanical properties of β-solidifying TiAl alloy fabricated by laser-engineered net shaping through heat treatment, Addit. Manuf. 67 (2023) 103502, https://doi.org/10.1016/j.addma.2023.103502.

[58] H. Zhu, Z. Wang, O. Muransky, J. Davis, S. Yu, D. Kent, G. Wang, M.S. Dargusch, The characterisation and formation of novel microstructural features in a Ti− Nb− Zr− Mo− Sn alloy manufactured by Laser Engineered Net Shaping (LENS), Addit. Manuf. 37 (2021) 101705, https://doi.org/10.1016/j.addma.2020.101705.

[59] M.M. Francois, A. Sun, W.E. King, N.J. Henson, D. Tourret, C.A. Bronkhorst, N. N. Carlson, C.K. Newman, T. Haut, J. Bakosi, J.W. Gibbs, Modeling of additive manufacturing processes for metals: Challenges and opportunities, Curr. Opin. Solid State Mater. Sci. 21 (2017) 198–206, https://doi.org/10.1016/j.cossms.2016.12.001.

[60] M.I. Al Hamahmy, I. Deiab, Review and analysis of heat source models for additive manufacturing, Int. J. Adv. Manuf. Technol. 106 (2020) 1223–1238, https://doi.org/10.1007/s00170-019-04371-0.

[61] S. Srivastava, R.K. Garg, V.S. Sharma, N.G. Alba-Baena, A. Sachdeva, R. Chand, S. Singh, Multi-physics continuum modelling approaches for metal powder additive manufacturing: a review, Rapid Prototyp. J. 26 (2020) 737–764, https://doi.org/10.1108/RPJ-07-2019-0189.

[62] F. Appel, J.D.H. Paul, M. Oehring, Gamma titanium aluminide alloys: science and technology, John Wiley & Sons, 2011.

[63] M. Kastenhuber, B. Rashkova, H. Clemens, S. Mayer, Enhancement of creep properties and microstructural stability of intermetallic β-solidifying γ-TiAl based alloys, Intermetallics 63 (2015) 19–26, https://doi.org/10.1016/j.intermet.2015.03.017.

[64] S.A. Raji, A.P.I. Popoola, S.L. Pityana, O.M. Popoola, Characteristic effects of alloying elements on β solidifying titanium aluminides: A review, Heliyon 6 (2020) 04463, https://doi.org/10.1016/j.heliyon.2020.e04463.

[65] M. Tlotleng, Microstructural properties of heat-treated LENS in situ additively manufactured titanium aluminide, J. Mater. Eng. Perform. 28 (2019) 701–708, https://doi.org/10.1007/s11665-018-3789-5.

[66] J. Jacob, 2020. Microstructures of TiAl Additively Manufactured by EBM and LMD (Doctoral dissertation). University of Melbourne.

[67] J.S. Keist, T.A. Palmer, Development of strength-hardness relationships in additively manufactured titanium alloys, Mater. Sci. Eng.: A 693 (2017) 214–224, https://doi.org/10.1016/j.msea.2017.03.102.

[68] W.C. Oliver, G.M. Pharr, An improved technique for determining hardness and elastic modulus using load and displacement sensing indentation experiments, J. Mater. Res. 7 (1992) 1564–1583, https://doi.org/10.1557/JMR.1992.1564.

[69] V. Verma, A. Mandal, A.J.I.J. Shukla, Laser direct metal deposition (LDMD)–An overview, Int. J. Adv. Res. Innov. 5 (2017) 459–467.

[70] L.R. Kanyane, P. Lepele, N. Malatji, M.B. Shongwe, 3D Finite Element Analysis and Experimental Correlations of Laser Synthesized AlCrNiTiNb High Entropy Alloy Coating, Mater. Today Commun. (2023) 107686, https://doi.org/10.1016/j.mtcomm.2023.107686.

[71] A. Klassen, V.E. Forster, V. Juechter, C. Körner, Numerical simulation of multi-component evaporation during selective electron beam melting of TiAl, J. Mater. Process. Technol. 247 (2017) 280–288, https://doi.org/10.1016/j.jmatprotec.2017.04.016.

[72] W. Ye, S. Zhang, L.L. Mendez, M. Farias, J. Li, B. Xu, P. Li, Y. Zhang, Numerical simulation of the melting and alloying processes of elemental titanium and boron powders using selective laser alloying, J. Manuf. Process. 64 (2021) 1235–1247, https://doi.org/10.1016/j.jmapro.2021.02.044.

[73] M. Balichakra, S. Bontha, P. Krishna, V.K. Balla, Prediction and validation of residual stresses generated during laser metal deposition of γ titanium aluminide thin wall structures, Mater. Res. Express 6 (2019) 106550, https://doi.org/10.1088/2053-1591/ab38ee.

[74] H.L. Wei, T. Mukherjee, W. Zhang, J.S. Zuback, G.L. Knapp, A. De, T. DebRoy, Mechanistic models for additive manufacturing of metallic components, Prog. Mater. Sci. 116 (2021) 100703, https://doi.org/10.1016/j.pmatsci.2020.100703.

[75] M.N. Mathabathe, S. Govender, A.S. Bolokang, R.J. Mostert, C.W. Siyasiya, Phase transformation and microstructural control of the α-solidifying γ-Ti-45Al-2Nb-0.7 Cr-0.3 Si intermetallic alloy, J. Alloy. Compd. 757 (2018) 8–15, https://doi.org/10.1016/j.jallcom.2018.05.051.

[76] M. Kastenhuber, T. Klein, H. Clemens, S. Mayer, Tailoring microstructure and chemical composition of advanced γ-TiAl based alloys for improved creep resistance, Intermetallics 97 (2018) 27–33, https://doi.org/10.1016/j.intermet.2018.03.011.

[77] T. Klein, B. Rashkova, D. Holec, H. Clemens, S. Mayer, Silicon distribution and silicide precipitation during annealing in an advanced multi-phase γ-TiAl based alloy, Acta Mater. 110 (2016) 236–245, https://doi.org/10.1016/j.actamat.2016.03.050.

[78] R.M. Imayev, V.M. Imayev, M. Oehring, F. Appel, Alloy design concepts for refined gamma titanium aluminide based alloys, Intermetallics 15 (2007) 451–460, https://doi.org/10.1016/j.intermet.2006.05.003.

[79] T. Klein, H. Clemens, S. Mayer, Advancement of compositional and microstructural design of intermetallic γ-TiAl based alloys determined by atom probe tomography, Materials 9 (2016) 755, https://doi.org/10.3390/ma9090755.

[80] C.J. Bettles, S. Tochon, M.A. Gibson, B.A. Welk, H.L. Fraser, Microstructure and mechanical properties of titanium aluminide compositions containing Fe, Mater. Sci. Eng.: A 575 (2013) 152–159, https://doi.org/10.1016/j.msea.2013.03.058.

[81] L. Chen, T.E.J. Edwards, F. Di Gioacchino, W.J. Clegg, F.P. Dunne, M.S. Pham, Crystal plasticity analysis of deformation anisotropy of lamellar TiAl alloy: 3D microstructure-based modelling and in-situ micro-compression, Int. J. Plast. 119 (2019) 344–360, https://doi.org/10.1016/j.ijplas.2019.04.012.

[82] F. Qiang, H. Kou, G. Yang, B. Tang, J. Li, Multi-step heat treatment design for nano-scale lamellar structures of a cast Ti-45Al-8.5 Nb-(W, B, Y) alloy, Intermetallics 79 (2016) 35–40, https://doi.org/10.1016/j.intermet.2016.09.006.

[83] E. Schwaighofer, H. Clemens, S. Mayer, J. Lindemann, J. Klose, W. Smarsly, V. Güther, Microstructural design and mechanical properties of a cast and heat-treated intermetallic multi-phase γ-TiAl based alloy, Intermetallics 44 (2014) 128–140, https://doi.org/10.1016/j.intermet.2013.09.010.

[84] M.N. Mathabathe, A.S. Bolokang, G. Govender, R.J. Mostert, C.W. Siyasiya, Structure-property orientation relationship of a γ/α2/Ti5Si3 in as-cast Ti-45Al-2Nb-0.7 Cr-0.3 Si intermetallic alloy, J. Alloy. Compd. 765 (2018) 690–699, https://doi.org/10.1016/j.jallcom.2018.06.265.

[85] L. Song, X.J. Xu, L. You, Y.F. Liang, J.P. Lin, Phase transformation and decomposition mechanisms of the βo (ω) phase in cast high Nb containing TiAl alloy, J. Alloy. Compd. 616 (2014) 483–491, https://doi.org/10.1016/j.jallcom.2014.07.130.

[86] F.S. Sun, F.S. Froes, Precipitation of Ti5Si3 phase in TiAl alloys, Mater. Sci. Eng.: A 328 (2002) 113–121, https://doi.org/10.1016/S0921-5093(01)01678-1.

[87] H.Z. Niu, Y.F. Chen, Y.S. Zhang, J.W. Lu, W. Zhang, P.X. Zhang, Phase transformation and dynamic recrystallization behavior of a β-solidifying γ-TiAl alloy and its wrought microstructure control, Mater. Des. 90 (2016) 196–203, https://doi.org/10.1016/j.matdes.2015.10.133.

[88] S.R. Dey, A. Hazotte, E. Bouzy, S. Naka, Development of Widmanstätten laths in a near-γ TiAl alloy, Acta Mater. 53 (2005) 3783–3794, https://doi.org/10.1016/j.actamat.2005.04.007.

[89] D. Huang, Q. Tan, Y. Zhou, Y. Yin, F. Wang, T. Wu, X. Yang, Z. Fan, Y. Liu, J. Zhang, H. Huang, The significant impact of grain refiner on γ-TiAl intermetallic fabricated by laser-based additive manufacturing, Addit. Manuf. 46 (2021) 102172, https://doi.org/10.1016/j.addma.2021.102172.

[90] T. Klein, M. Schachermayer, F. Mendez-Martin, T. Schöberl, B. Rashkova, H. Clemens, S. Mayer, Carbon distribution in multi-phase γ-TiAl based alloys and its influence on mechanical properties and phase formation, Acta Mater. 94 (2015) 205–213, https://doi.org/10.1016/j.actamat.2015.04.055.

[91] T.K. Lee, E.I. Mosunov, S.K. Hwang, Consolidation of a gamma TiAl–Mn–Mo alloy by elemental powder metallurgy, Mater. Sci. Eng.: A 239 (1997) 540–545, https://doi.org/10.1016/S0921-5093(97)00628-X.

[92] M.L. Oyen, R.F. Cook, A practical guide for analysis of nanoindentation data, J. Mech. Behav. Biomed. Mater. 2 (2009) 396–407, https://doi.org/10.1016/j.jmbbm.2008.10.002.

[93] B. Lerch, S. Draper, M. Pereira, W. Zhuang, 2003. January. Durability Assessment of Various Gamma TiAl Alloys. In: proceedings of the 2003 TMS Annual Meeting & Exhibition: 3rd International Symposium on Gamma Titanium Aluminides, San Diego, CA, USA:1-7.

[94] H. Clemens, W. Wallgram, S. Kremmer, V. Güther, A. Otto, A. Bartels, Design of novel β-solidifying TiAl alloys with adjustable β/B2-phase fraction and excellent hot-workability, Adv. Eng. Mater. 10 (2008) 707–713, https://doi.org/10.1002/adem.200800164.

[95] S.J. Qu, S.Q. Tang, A.H. Feng, C. Feng, J. Shen, D.L. Chen, Microstructural evolution and high-temperature oxidation mechanisms of a titanium aluminide based alloy, Acta Mater. 148 (2018) 300–310, https://doi.org/10.1016/j.actamat.2018.02.013.

[96] Z.W. Huang, Thermal stability of Ti-44Al-4Nb-4Hf-0.2 Si-1B alloy, Intermetallics 37 (2013) 11–21, https://doi.org/10.1016/j.intermet.2013.01.011.

[97] M. Mitoraj-Królikowska, E. Godlewska, Silicide coatings on Ti-6Al-1Mn (at%) alloy and their oxidation resistance, Surf. Coat. Technol. 334 (2018) 491–499, https://doi.org/10.1016/j.surfcoat.2017.12.004.

[98] O. Ostrovskaya, C. Badini, G. Baudana, E. Padovano, S. Biamino, Thermogravimetric investigation on oxidation kinetics of complex Ti-Al alloys, Intermetallics 93 (2018) 244–250, https://doi.org/10.1016/j.intermet.2017.09.020.

[99] N.A. Nochovnaya, P.V. Panin, A.S. Kochetkov, K.A. Bokov, Modern refractory alloys based on titanium gamma-aluminide: prospects of development and application, Met. Sci. Heat. Treat. 56 (2014) 364–367, https://doi.org/10.1007/s11041-014-9763-4.